

Engineering

Prof. David L. Carroll Wake Forest University, USA



Journal Editorial Board

ISSN: 1947-3931 (Print), 1947-394X (Online)

<http://www.scirp.org/journal/eng>

Editor-in-Chief

Prof. David L. Carroll

Wake Forest University, USA

Editorial Board

Prof. Alain. Bernard

Ecole Centrale de Nantes, France

Prof. Hongbin Sun

Tsinghua University, China

Prof. Chengshan Wang

Tianjin University, China

Prof. Xiangjun Zeng

Changsha University of Science and Technology, China

Prof. Luowei Zhou

Chongqing University, China

Dr. Hongyu Zhang

Ceres Inc., Thousand Oaks, CA, USA

Dr. Wei Yan

Trend Micro, USA

Dr. Hongyang Chen

The University of Tokyo, Japan

Prof. Ming Chen

Southeast University, China

Prof. Chui-Chi Lee

SHU-TE University, Taiwan (China)

Prof. Zhao Xu

Technical University of Denmark, Denmark

Prof. Jae MOUNG Kim

INHA University Incheon, Korea (South)

Prof. Baolin Wang

Harbin Institute of Technology, China

Prof. Shahnor Basri

Universiti Putra Malaysia Selangor, Malaysia

Prof. Tsutomu Yoshihara

Waseda University, Japan

Prof. John Marsh

IEEE Photonics Society, UK

Prof. Gaofeng Wang

Wuhan University, China

Dr. Koduri Venkata Surya Ramam

Universidad of Concepcion, Chile

Dr. Rahat Iqbal

Coventry University, UK

Dr. Rehan Ahmed

Heriot-Watt University, UK

Dr. P. Chandramohan

Anna University, India

Dr. Mehrdad Massoudi

U. S. Department of Energy/NETL-Pittsburgh, USA

Prof. MOH'D A. M. AL-NIMR

Jordan University of Science and Technology, Jordan

Dr. V.P. Yashnikov

Russian Academy of Sciences, Russia

Prof. Yong-Gang Lv

Chongqing University, China

Prof. Jan Awrejcewicz

Department of Automatics and Biomechanics (DAB), TUL, Poland

Prof. Shouetsu Itou

Kanagawa University, Japan

Prof. Sergey M. Smolskiy

Moscow Power Engineering University, Russia

Editorial Assistant

Zhenhua Sun

Scientific Research Publishing, USA

eng@scirp.org

Guest Reviewers

Marcelo A. Savi

Bo Chen

Jamshid Aghaei

Mehdi Roopaei

Krzysztof Gorecki

Song Cen

Ihsan Kaya

Muhsin Gencoglu

Sangjin Ryoo

Yi Zhang

N. Belhaouchet

S. C. Wu

E. J. Solteiro Pires

drien Plecis

Naotake Noda

Hassan Zohoor

Angeliki Tserepi

Jianzhong ZHOU

Jun Ye

Jochen Mahlib

Herman Clercx

Peter Vorobieff

TABLE OF CONTENTS

Volume 2 Number 2

February 2010

Experimental Study of Stacked Rectangular Microstrip Antenna for Dual-Band R. K. Vishwakarma, S. Tiwari.....	85
Analysis of Rectangular Notch Antenna for Dual-Band Operation R. K. Vishwakarma, S. Tiwari.....	91
The Quantized Characterization of Cooked Rice Hardness and Research on the Automatic Measurement Technology N. Jiang, Y. Gao, J. P. Zhou, L. Q. Gao, J. H. Zhou, Q. G. Dai.....	97
Analytic Computation Method of the Equivalent Thickness of Superposition Multi-Throttle-Slices of Twin-Tubes Shock Absorber C. C. Zhou, Y. Z. Xu.....	103
Sliding Mode Control with Auto-Tuning Law for Maglev System L. L. Zhang, Z. Z. Zhang, Z. Q. Long, A. Hao.....	107
The Research on Adaptive Control Modeling of a Liquid Fertilizer Spreader Z. D. Yang.....	113
A Set of Globally Stable N-PID Regulators for Robotic Manipulators B. S. Liu, F. C. Lin, B. L. Tian	118
Focusing of Azimuthally Polarized Hyperbolic-Cosine-Gaussian Beam X. M. Gao, M. Y. Gao, S. Hu, H. M. Guo, J. Wang, S. L. Zhuang.....	124

Engineering

Journal Information

SUBSCRIPTIONS

Engineering (Online at Scientific Research Publishing, www.SciRP.org) is published quarterly by Scientific Research Publishing, Inc., USA.

E-mail: eng@scirp.org

Subscription rates: Volume 2 2010

Print: \$50 per copy.

Electronic: free, available on www.SciRP.org.

To subscribe, please contact Journals Subscriptions Department, E-mail: eng@scirp.org

Sample copies: If you are interested in subscribing, you may obtain a free sample copy by contacting Scientific Research Publishing, Inc at the above address.

SERVICES

Advertisements

Advertisement Sales Department, E-mail: eng@scirp.org

Reprints (minimum quantity 100 copies)

Reprints Co-ordinator, Scientific Research Publishing, Inc., USA.

E-mail: eng@scirp.org

COPYRIGHT

Copyright© 2010 Scientific Research Publishing, Inc.

All Rights Reserved. No part of this publication may be reproduced, stored in a retrieval system, or transmitted, in any form or by any means, electronic, mechanical, photocopying, recording, scanning or otherwise, except as described below, without the permission in writing of the Publisher.

Copying of articles is not permitted except for personal and internal use, to the extent permitted by national copyright law, or under the terms of a license issued by the national Reproduction Rights Organization.

Requests for permission for other kinds of copying, such as copying for general distribution, for advertising or promotional purposes, for creating new collective works or for resale, and other enquiries should be addressed to the Publisher.

Statements and opinions expressed in the articles and communications are those of the individual contributors and not the statements and opinion of Scientific Research Publishing, Inc. We assumes no responsibility or liability for any damage or injury to persons or property arising out of the use of any materials, instructions, methods or ideas contained herein. We expressly disclaim any implied warranties of merchantability or fitness for a particular purpose. If expert assistance is required, the services of a competent professional person should be sought.

PRODUCTION INFORMATION

For manuscripts that have been accepted for publication, please contact:

E-mail: eng@scirp.org

Experimental Study of Stacked Rectangular Microstrip Antenna for Dual-Band

Rajesh Kumar Vishwakarma¹, Sanjay Tiwari²

School of Studies in Electronics, Pt. Ravishankar Shukla University, Raipur, Chhattisgarh (C.G)

E-mail: rkv_786@yahoo.com, drsanjaytiwari@gmail.com

Received August 27, 2009; revised September 14, 2009; accepted September 20, 2009

Abstract

A dual-band characteristic of stacked rectangular microstrip antenna is experimentally studied. It is a probe fed antenna for impedance matching with 50Ω coaxial cable. This antenna works well in the frequency range (2.86 to 4.63 GHz). It is basically a low cost, light weight medium gain antenna, which is used for mobile communication. The variations of the length and width (1mm) of the stacked rectangular patch antenna have been done. And it is found dual resonance with increasing lower resonance frequency and almost constant upper resonance frequency with increases of the length & width of rectangular microstrip antenna. The input impedance and VSWR, return loss have been measured with the help of Network analyzer.

Keywords: Microstrip Antenna, Stacked Patch Antenna, Dual-Band Antenna, Network Analyzer, Bandwidth

1. Introduction

The demand for application of microstrip antenna in various communication systems has been increasing rapidly due to its lightweight, low cost, small size, ease of integration with other microwave components [1–4]. Microstrip antenna gained in popularity and become a major research topic in both theoretically and experimentally. However one of main disadvantages of microstrip antenna is their narrow band width. It is well known that the multilayer structure is useful method to improve these problems. The researcher have investigated their basic characteristics and extensive efforts have also been developed to design of electromagnetically coupled two layer elliptical microstrip stacked antenna [5], stacked square patch antenna for Bluetooth application [6] and analysis of stacked microstrip rectangular microstrip antenna [7]. Several methods have been presented in the last years to improve it's such as: thicker substrate [8] reactive matching network [9], and stacked patches [10–12]. Microstrip patch antenna elements with a single feed are used in many popular for various radar and communication system such as synthetic aperture radar (SAR), dual-band, multi-band, mobile communication system and Global Positioning Systems (GPS) [13]. It may be mentioned that the bandwidth can also be improved by stacking a parasitic patch on the fed patch [14]. Therefore in this present paper, we observed on an electromagnetically stacked rectangular microstrip antenna

with number of parasitic elements. By using two stacked patches with the wall at edges between the two patches, one can obtained enhance impedance bandwidth. Experimental work is carried out to study the effect of stacking on various parameters of antenna.

2. Antenna Design Calculation

The transmission line model is used to design rectangular microstrip antenna which is stacked one by one. Rectangular microstrip antenna (RMA) is designed by using following procedures.

2.1. Patch Width and Patch Length

The first to design the patch is choosing a suitable dielectric substrate of suitable thickness. For rectangular microstrip antenna, the width W and the length L depends on the resonant frequency f_r and the parameters of the substrate employed [1].

To design the rectangular patch width of the antenna is given by

$$W = \frac{c}{2 \cdot f_r} \left[\left(\frac{\epsilon_r + 1}{2} \right) \right]^{-\frac{1}{2}} \quad (1)$$

where C = velocity of light

W = width of the microstrip patch

ϵ_r = Dielectric constant of the substrate Length of the resonant element is given by

$$L = \frac{c}{2 \cdot f_r \sqrt{\epsilon_{eff}}} - 2\Delta l \tag{2}$$

where

ϵ_{eff} = Effective dielectric constant of the substrate

Δl = Line extension

ϵ_{eff} and Δl can be expressed as

$$\epsilon_{eff} = \left(\frac{\epsilon_r + 1}{2}\right) + \left(\frac{\epsilon_r - 1}{2}\right) \cdot \left(1 + \frac{10 \cdot h}{W}\right)^{-0.5}$$

$$\Delta l = 0.412h \left[\frac{0.262 + \frac{W}{h}}{0.813 + \frac{W}{h}} \right] \left[\frac{\epsilon_{eff} + 0.3}{\epsilon_{eff} - 0.258} \right]$$

where, h is the thickness of the substrate.

The driven patches were designed to operate at a resonant frequency of 3.0 GHz, their length and width were calculated to be $L= 23.01\text{mm}$ and width $W= 30.01\text{mm}$ respectively. The remaining five patches were designed with the differences of 1mm in the length and width with increasing mode. They are stacked in the manner shown in (Figure 1).

2.2. Feeding Design

The feeding point was designed for lower patch to match the (50 Ω) coaxial cable feed and the patch. The feeding point was fabricated along the length of the patch. The input conductance of the patch fed on the edge slot will be twice the conductance of one of the edge slots as suggested by Harrington and given by [15].

$$G = \frac{\pi W}{\eta \lambda_0} \left[1 - \frac{(kh)^2}{24} \right] \tag{3}$$

where $\eta = 120\pi$ $k = \frac{2\pi}{\lambda_0}$ $\lambda_0 =$ Wavelength of free space

So the input impedance of the patch is given by

$R_I = 1/2G$ (Ω), where G is radiation conductance.

So the upper patch is parasitic and the lower patch is fed with a co axial probe at the position (X_0, Y_0) where $X_0=$

6.40 mm and $Y_0= 15.725$ mm. All the designed patches have been stacked one over the driven patch.

3. Experimental Measurements

The rectangular microstrip antenna was measured using network analyzer [Agilent E8363B A.04.06]. For obtaining the desired dual-frequency behavior the lower patch conductor of the coaxial feed is allowed to pass through a clearance hole in the lower patch and is then eclectically connected to the upper patch as shown in (Figure 1). The rectangular microstrip consists of one driven patch and five parasitic patches designed for 3.0 GHz. The variation of length and width with design frequencies of antennas are shown in the Table 1. The

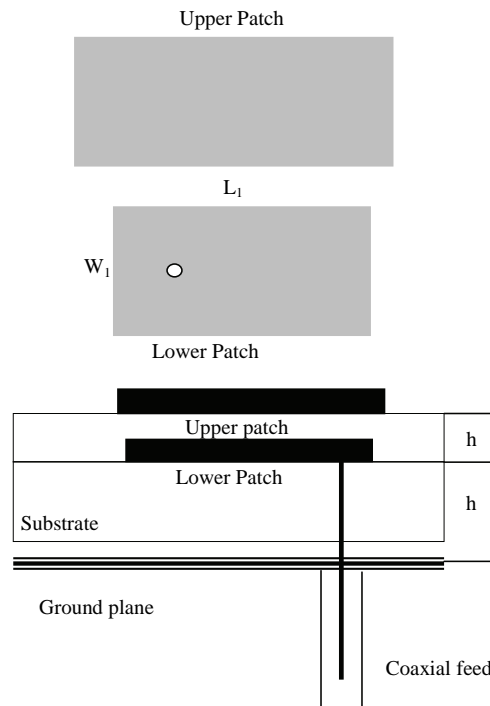


Figure 1. The dual-band electromagnetically coupled stacked antenna. (a) Upper patch and Lower patch; (b) Cross section.

Table 1. variation of length and width with design frequencies of patches.

Patches in mm	Dimension of patch Length and width (mm)	Design frequency in GHz
Antenna (Driven patch)	23.01 x 30.15	3.0
Patch 1	24.01 x 31.15	3.0
Patch 2	25.01 x 32.15	3.0
Patch 3	26.01 x 33.15	3.0
Patch 4	27.01 x 34.15	3.0
Patch 5	28.01 x 35.15	3.0

Table 2. Variation of upper and lower resonance frequencies and their ratio (f_2/f_1) with return loss in dB.

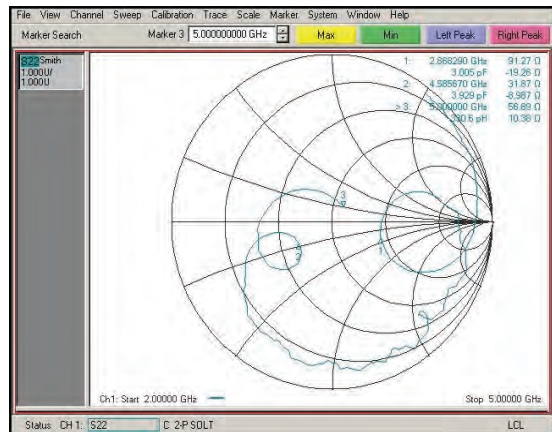
Patches in mm	Lower resonance frequency f_1 (GHz)	Upper resonance frequency f_2 (GHz)	Ratio of resonance frequencies f_2 / f_1 (GHz)	Return loss(dB) for f_1 (GHz)	Return loss(dB) for f_2 (GHz)
Patch 1	2.868	4.585	2.868	-9.99	-12.24
Patch 2	2.904	4.625	2.904	-11.85	-14.24
Patch 3	2.903	4.593	2.903	-10.89	-12.65
Patch 4	2.917	4.624	2.917	-13.26	-14.46
Patch 5	2.917	4.636	2.917	-13.80	-14.45

variation of upper and lower resonance frequencies and their ratio (f_2/f_1) with increasing patch length and width are shown in the Table 2. In order to study the performance of the development rectangular microstrip antenna return loss, resonance frequencies and VSWR were measured experientially with different number of parasitic antenna shown in the Table 2. The broad band width is achieved about 45% with the stacking of the antenna.

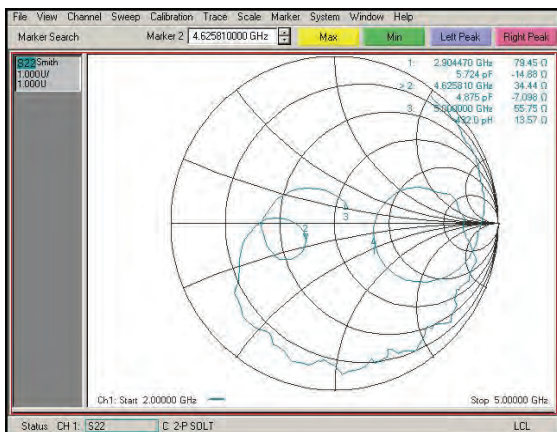
4. Design Parameters

The various design parameters of the antenna are as follows:

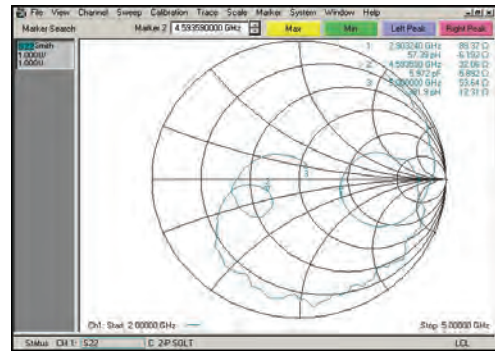
- Substrate material used Glass Epoxy
- Thickness of the dielectric substrate $h = 1.59$ mm



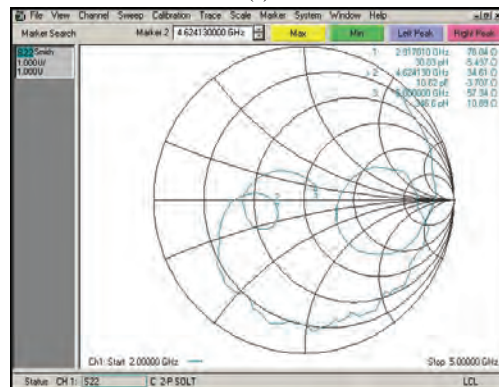
(a)



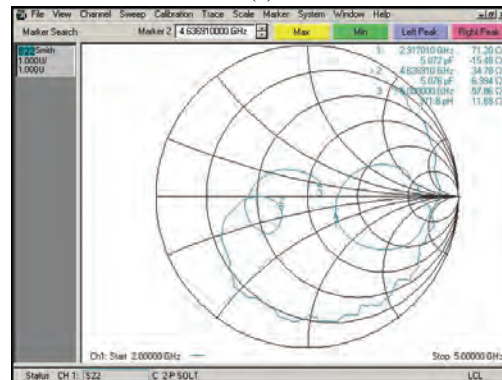
(b)



(c)

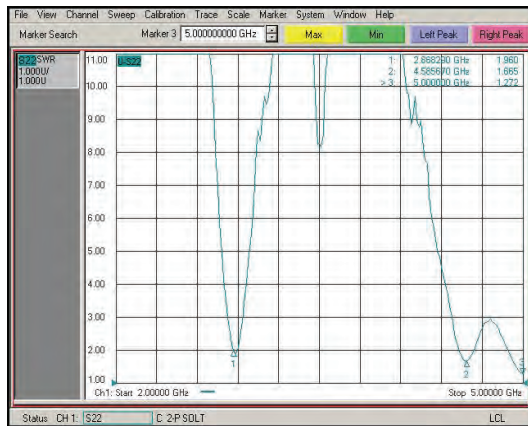


(d)

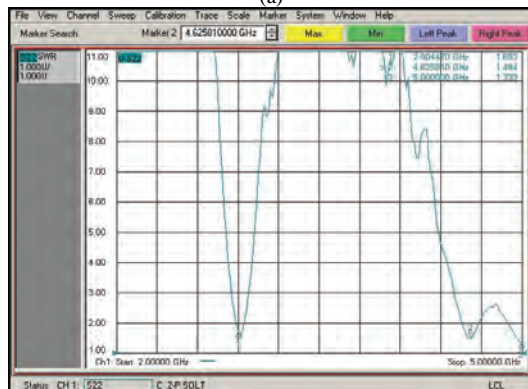


(e)

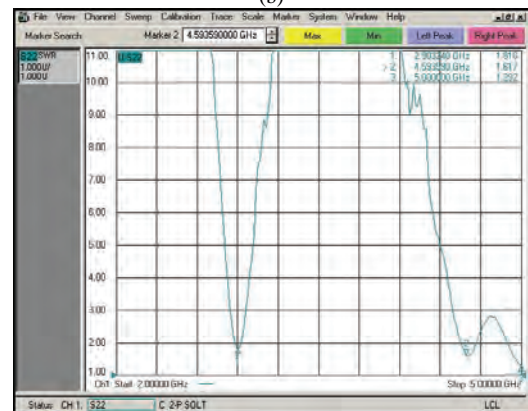
Figure 2. (a) Variations of input impedance with frequency for patch dimension 24.01x 31.15; (b) Variations of input impedance with frequency for patch dimension 25.01x 32.15; (c) Variations of input impedance with frequency for patch dimension 26.01x 33.15; (d) Variations of input impedance with frequency for patch dimension 27.01x 34.15; (e) Variations of input impedance with frequency for patch dimension 28.01x 35.15.



(a)



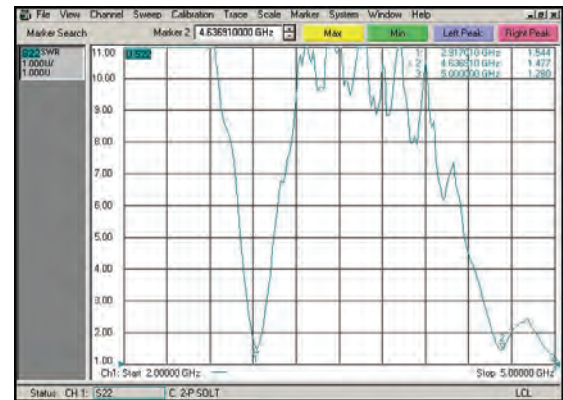
(b)



(c)



(d)



(e)

Figure 3. (a) Variations of VSWR with frequency for patch dimension 24.01x 31.15; (b) Variations of VSWR with frequency for patch dimension 25.01x 32.15; (c) Variations of VSWR with frequency for patch dimension 26.01x 33.15; (d) Variations of VSWR with frequency for patch dimension 27.01x 34.15; (e) Variations of VSWR with frequency for patch dimension 28.01x 35.15.

Relative permittivity of the substrate $\epsilon_r = 4$.

Design frequency $f = 3.0$ GHz

Thickness of the patch $t = 0.0018$ cm

And designed values were calculated using the standard equations, which are given below.

The width of the rectangular patch (Driven Patch) $W_1 = 30.15$ mm.

The length of the rectangular patch (Driven Patch) $L_1 = 23.01$ mm.

The variation of length of the patch (Parasitic Patch) $L = 24.01$ mm to 28.01 mm.

The variation of width length of the patch (Parasitic Patch) $W = 31.15$ mm to 35.15 mm.

5. Discussion of Results

1) The variation of input impedance with frequency for rectangular dimensions (Patch 1 to Patch 5) is shown in Figures 2(a) to 2(e). It is observed that stacked patch antenna shows dual resonance in which lower resonance frequency increases with increasing patch dimensions where as at the upper resonance frequencies increase with increasing the patch dimensions.

2) The variation of VSWR with frequency for rectangular dimensions (Patch 1 to Patch 5) is shown in Figures 3(a) to 3(e) It is observed that the value of VSWR corresponding to lower resonance frequency is decreases from 1.96 to 1.54 with increasing patch dimensions where as at the upper resonance frequency the value of VSWR is also decrease from 1.66 to 1.47.

3) The variation of resonance frequencies with different dimensions of the antenna (Patch 1 to Patch 5) are shown in the Figure 4, It is observed that both resonance frequencies increase with increasing the patch dimensions.

4) The variation of resonance frequency ratio f_2/f_1 with dimensions of the antenna (Patch 1 to Patch 5) is shown

in the Figure 5. It is observed that both ratios of resonance frequencies are all most constant with increasing the patch dimensions.

5) The variation of different dimensions of the antenna (Patch 1 to Patch 5) with real part of input impedance is shown in Figure 6. It is observed that the real part of input impedance is decrease from 91.27 to 71.20 at lower resonance frequency and increases as 31.87 to 34.78 with increasing the patch dimensions.

6. Conclusions

This paper has investigated the effect of introducing di-

mensions variation of parasitic patches on the performance of an electromagnetically coupled stacked rectangular microstrip antenna. The dual-band operation is achieved. It is observed from the experimental result that the resonance frequencies ratio all most constant (2.86 to 2.91 GHz) with increasing the patch dimensions. The broad band width is also achieved 45% of the rectangular microstrip antenna by stacking the patches. Therefore the proposed antenna can be used for mobile communication, where as upper resonance frequency is almost constant with increasing the patch dimensions.

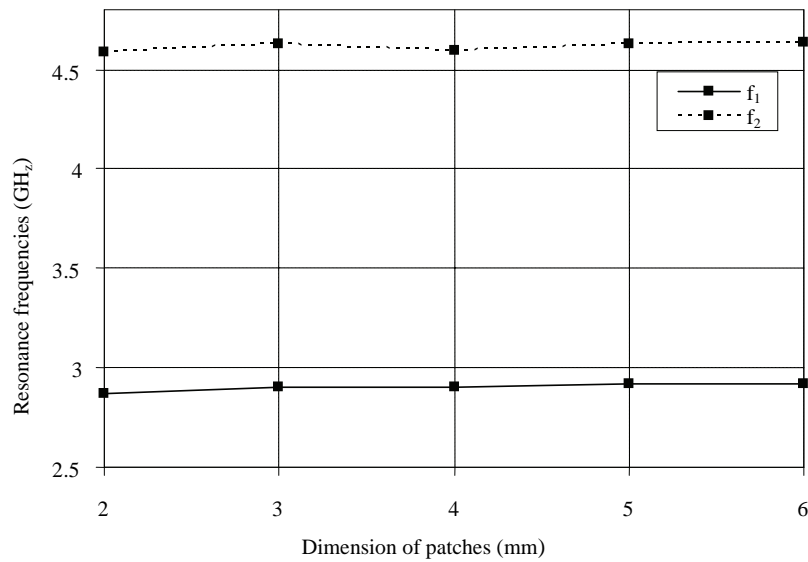


Figure 4. Variation of resonance frequencies with different patch dimensions.

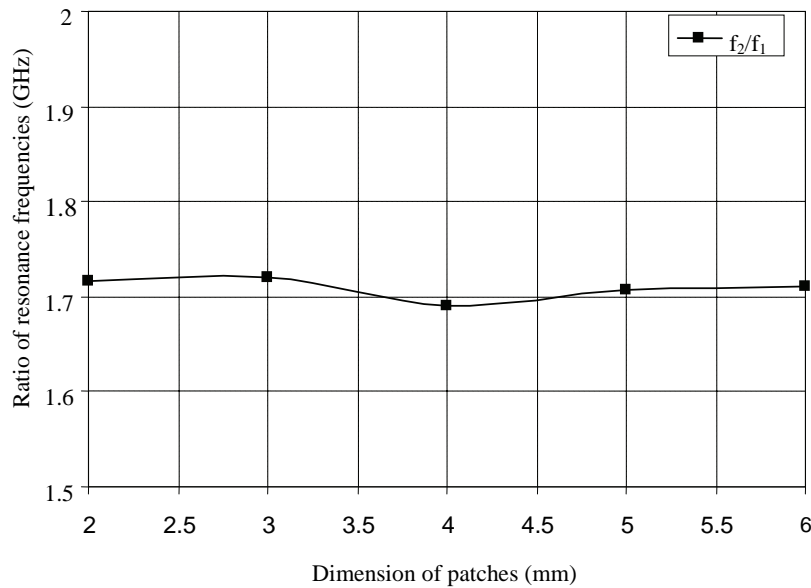


Figure 5. Variation of ratio resonance frequencies with different patch dimensions.

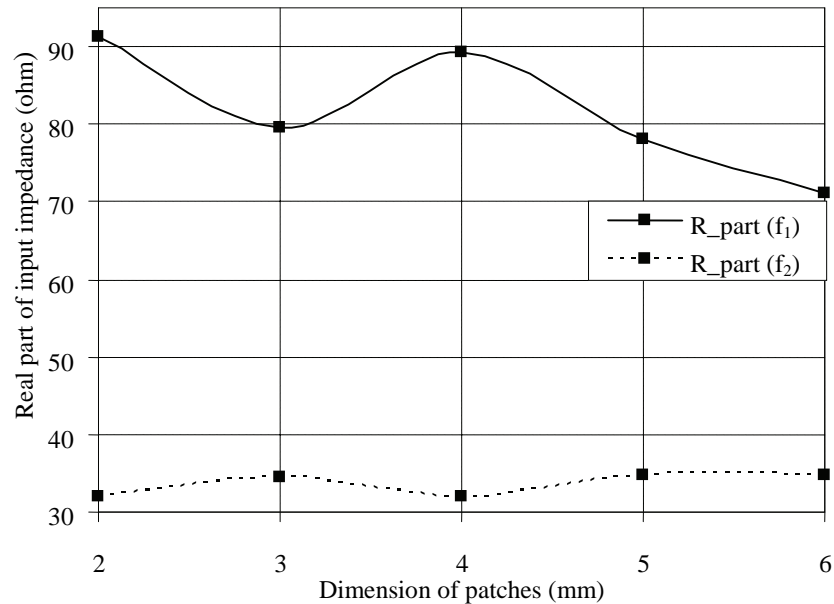


Figure 6. Variations of patch dimensions with real part of input impedance.

7. Acknowledgments

The authors would like to thank Professors Arun Kumar and Shri R. K. Malaviya of the Space Application Centre, Indian Space Research Organization Ahmedabad, for providing the measurement facilities.

8. References

- [1] J. I. Bahl, and P. Bhartia, *Microstrip Antennas*, Dedham, MA, (USA) Artech House, 1980.
- [2] J. R. James, P. S. Hall, and C. Wood, "Microstrip antenna theory and design" *IEE Electromagnetic Wave, Series 12* London, U. K. Peter Peregrinus, 1981.
- [3] K. C. Gupta, "Recent advance in microstrip antenna," *Microwave Journal*, No. 27, pp. 50–67, 1984.
- [4] S. A. Long and M. D. Walton, "A dual-frequency circular-disc antenna," *IEEE Transactions on Antenna and Propagation USA*, AP-27, pp. 270–273, 1979.
- [5] R. L. Yadava and B. R. Vishvakarma, "Analysis of electromagnetically coupled two-layer elliptical microstrip stacked antennas," *International Journal of Electronics*, Vol. 87, No. 8, pp. 981–993, 2000.
- [6] A. B. Nandgaonkar and S. B. Deosarkar, "Broadband stacked patch antenna for bluetooth applications," *Journal of Microwaves, Optoelectronics and Electromagnetic Application*, Vol. 8, No. 1, pp. 1–5, 2009.
- [7] I. K. Moussa and D. A. E. Mohamed and I. badran, "Analysis of stacked rectangular microstrip antenna," 24th National Radio Science Conference, March 13-15, pp. 1–10, 2007.
- [8] W. Chen, K. F. Lee, and R. O. Lee, "Input impedance of coaxially fed rectangular microstrip antenna on electrically thick substrate," *Microwave optical Technology Letters*, Vol. 6, No. 6, pp. 387–390, 1993.
- [9] F. Pues and R. Van De Capelle, "An impedance matching technique for increasing the bandwidth of microstrip antenna," *IEEE Transactions on Antennas Propagation*, Vol. 37, pp. 1345–1354, 1989.
- [10] J. S. Dahele and K. F. Lee, "A dual-frequency stacked microstrip antenna," *IEEE AP-S International Symposium Digest*, pp. 308–30–11, 1982.
- [11] K. F. Lee, K. Y. Ho, and J. S. Dahele, "Circular-disk microstrip antenna with air gap", *IEEE Transactions on Antenna (USA) and Propagation*, AP-32, pp. 880–884, 1984.
- [12] J. S. Dahele, K. F. Lee, and D. P. Wong, "Dual frequency stacked annular ring microstrip antenna," *IEEE Transactions Antennas and Propagation (USA) AP-35*, pp. 1281–1285, 1987.
- [13] D. M. Pozar and S. M. Duffy. "A dual-band circular polarized aperture-coupled stacked microstrip antenna for global positioning satellite," *IEEE Transactions on Antennas and Propagation (USA)*, Vol. 45, No. 11, pp. 1618–1625, 1997.
- [14] S. Egashira and E. Nishiyama "Stacked microstrip antenna with wide bandwidth and high gain," *IEEE Transactions on Antennas and Propagation (USA) Vol. 44*, No. 11, pp. 1533–1534, 1996.
- [15] R. E. Harrington, "Time harmonic electromagnetic field," Ms Graw-Hill, New Delhi, 1979.

Analysis of Rectangular Notch Antenna for Dual-Band Operation

Rajesh Kumar Vishwakarma¹, Sanjay Tiwari²

School of Studies in Electronics, Pt. Ravishankar Shukla University, Raipur, Chhattisgarh (C.G)

E-mail: rkv_786@yahoo.com, drsanjaytiwari@gmail.com

Received August 27, 2009; revised September 14, 2009; accepted September 20, 2009

Abstract

In this paper a design of single layer rectangular notch microstrip antenna for dual-band is proposed and experimentally investigated. This antenna is excited by microstrip line. Direct microstrip coupling with proper matching transformer has been used. Design is made for optimized notch dimension for two resonant frequencies. These resonance frequencies change with the variation in length and width of the notch. The input impedance and VSWR have been measured with the help of Network analyzer. It is found that the input impedance and VSWR depends variation in length and width of the notch microstrip antenna.

Keywords: Microstrip Antenna, Notch Antenna, Dual-Band Antenna, Matching Transformer

1. Introduction

Microstrip antennas are receiving much attention at present because they offer many practical advantages such as small size, lightweight, low cost and a low profile ease of fabrication and integration with RF devices [1]. In the recent years, radar, satellite communication wireless networks such as global positioning system (GPS), synthetic aperture radar (SAR), often require dual frequency patch antenna to avoid the use of two different antennas. An ideal dual-frequency antenna should have similar performance in both operating modes. One of the principal disadvantages of such antenna is narrow bandwidth. Recently several papers [2-4] have been published treating notch microstrip antenna to achieve dual band characteristics. The major limitation of microstrip antenna lies in its limited bandwidth. Several methods have been reported in the literature [5-7] to improve the bandwidth of the microstrip antenna such as thicker substrate use of parasitic elements, proximity coupling of the feed line, and stacked microstrip antennas. Recently Palit [8] et al has reported a microstrip antenna by properly cutting a notch inside the radiating element. This properly fields enough BW for dual band frequency and broadband operation. In this case dual resonance is obtained by a dipole loaded notch antenna [9], notch loaded patch antenna [10], and notch triangular microstrip antenna [11] at the radiating edge of patch. The idea is extended by designing variation of length and width of the notch antenna. In the present work, and the effect of notch length and width on

the resonance frequencies have been carried out.

2. Feeding Network

The microstrip line method is easy to fabricate simple to model and match by controlling the inset cut position in the patch in the (Figure 1). Matching transformers transform the input resistance of patch to 50 ohm coaxial cable. The ratio W/h of the microstrip line used for feeding network can patch to found as to follows. The effective dielectric constant change with the ratio of strip width W to thickness h as [12]

$$\epsilon_{eff} = \left(\frac{\epsilon_r + 1}{2} \right) + \left(\frac{\epsilon_r - 1}{2} \right) \cdot \left(1 + \frac{10 \cdot h}{w} \right)^{-0.5} \quad (1)$$

when then define

$$Z_o = Z \sqrt{\epsilon_{eff}} \quad (2)$$

where Z is the strip impedance. The formula for Z_o for $W/h \leq 1$ can be given as

$$Z_o = 60 \ln \left(\frac{8H}{w} + \frac{w}{4h} \right) \text{ for } \frac{W}{h} \leq 1 \quad (3)$$

$$Z_o = \frac{120\pi}{\frac{W}{h} + 2.42 - 0.44 \frac{h}{W} \left(1 - \frac{h}{W} \right)^6} \text{ for } \frac{W}{h} > 1 \quad (4)$$

We can find the impedance when W/h is known but most design problem required the otherwise i.e. give Z

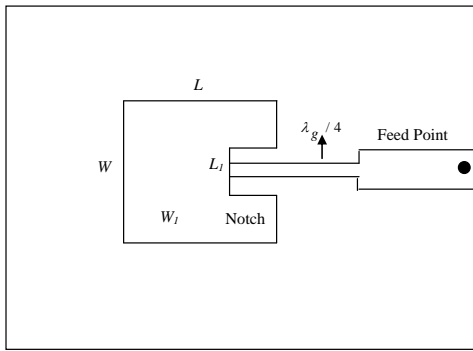


Figure 1. The notch rectangular microstrip antenna.

fin W/h , So Equations (1) and (3) or (4) in an interactive process are used to find W/h when $W/h = 1$, We first find Z_0 of $W/h = 1$ and then ϵ_{eff} and impedance are calculated as.

$$\epsilon_{eff} = \left(\frac{\epsilon_r + 1}{2} \right) + \left(\frac{\epsilon_r - 1}{2} \right) \frac{W}{h} = 1 \quad (5)$$

$$Z_o = Z\sqrt{\epsilon_{eff}}$$

and

$$Z_o = Z\sqrt{\epsilon_{eff}} \quad (6)$$

where

$$Z_o = 126.6 \left(\frac{W}{h} = 1 \right)$$

If Z_o is greater than Z_o (1) then W/h using is less or equal 1

Case 1 When $\frac{W}{h} \leq 1$ then

$$\frac{W}{h} = 2 \left(\exp\left(\frac{Z_o}{60}\right) - \sqrt{\left[\exp\left(\frac{Z_o}{60}\right)\right]^2 - 8} \right) \quad (7)$$

starting with ϵ_{eff} (1) we solve for $\frac{W}{h}$ using this value. We find $\epsilon_{eff}\left(\frac{W}{h}\right)$ from equation. Then it is substituted back in 13 to find a new value of $\frac{W}{h}$

Case 2 when $\frac{W}{h} > 1$ we use Newton's method of the finding function zero to form an integration equation.

Let $X = \left(\frac{W}{h}\right)$

$$\left(\frac{W}{h}\right)_{new} = X \left[\frac{1 - X^2 + X \left(2.42 + \left(1 - \frac{1}{X}\right)^6 - \frac{120\pi}{Z_o} \right)}{X^2 + 0.44 + 6 \left(1 - \frac{1}{X}\right)^5} \right] - 0.44 \quad (8)$$

using the new $\frac{W}{h}$ we find $\epsilon_{eff} \frac{W}{h}$ and a new value of Z_0 . A good starting value for the iteration is found from

$$\frac{W}{h} = \frac{120}{Z_0} - 198 \quad (9)$$

Iteration method has been done from Equations 1 to 9 and converges in a few cycles.

3. Measurement Techniques

The network analyzer is used to perform the measurement. Glass epoxy substrate with thickness of $h=1.59$ mm and approximate dielectric constant $\epsilon_r = 4.5$ was used. Several patches were fabricated with the variation of notch length and width. The variation of lower and upper resonance frequencies with notch length and width are shown in the Figures 6(a) and 6(b). The variation of upper and lower resonance frequencies ratio (f_2/f_1) with notch length and width are shown in the Figures 7(a) and 7(b). The resulting data are shown in Tables 1 to 2.

4. Design Procedure and Design Parameters

The actual dimension of the antenna designed is magnified two times in order to achieve the desired accuracy in the final design. The antenna shape of enlarged dimension is taken times in rubyolith film. This enlarge shape is photo reduced using a high precision camera to produce a high-resolution negative, which is later used for exposing the photo resist. The laminate is cleaned to insure proper adhesion of the photo resist and necessary resolution in the photo development process. The photo resist is now applied to both sides of the laminate using a laminator. After wards, the laminate is allowed to stand to normalize to room temperature prior to exposure and development. The photographic negative is now held in a very close contact with the cover sheet of the applied

Table 1. Variation of resonance frequencies with notch length for a given width =10mm.

Length (mm)	Frequency (f_1) GHz	Frequency (f_2) GHz	Frequencies ratio (f_2/f_1) GHz
2	2.998	4.525	1.527
3	2.993	4.606	1.613
4	3.01	4.523	1.513
5	3.01	4.619	1.609

Table 2. Variation of resonance frequencies with notch width for a given length =2mm.

Width (mm)	Frequency (f_1) GHz	Frequency (f_2) GHz	Frequencies ratio (f_2/f_1) GHz
6	2.955	4.497	1.542
7	2.930	4.522	1.592
8	2.953	4.534	1.581
9	2.962	4.535	1.572

photo resist, to assure the fine line resolution required with exposure to proper wave length light, polymerization of the exposed photo resist occurred, making it insoluble in developer solution. The backside of the antenna is completely exposed without a mask, since the copper foil is retained to act as a ground plane. The protective cover sheet of the photo resist is removed and the antenna is now developed in developer, which remove the soluble photo resist material.

Then the antenna is etched. Visual inspection is used to assure proper etching. Then excess photo resist is removed using a stripping solution. For stack antenna, the passive antenna are made with single side PCB same as done for active antenna.

The various design parameters of the antenna are as follows:

Substrate material used Glass Epoxy

Thickness of the dielectric substrate $h = 1.59$ mm

Relative permittivity of the substrate $\epsilon_r = 4.5$

Design frequency $f = 3.0$ GHz

Thickness of the patch $t = 0.0018$ cm and designed values were calculated using the standard equations, which are

The width of the rectangular patch $W = 30.15$ mm

The length of the rectangular patch $L = 23.04$ mm

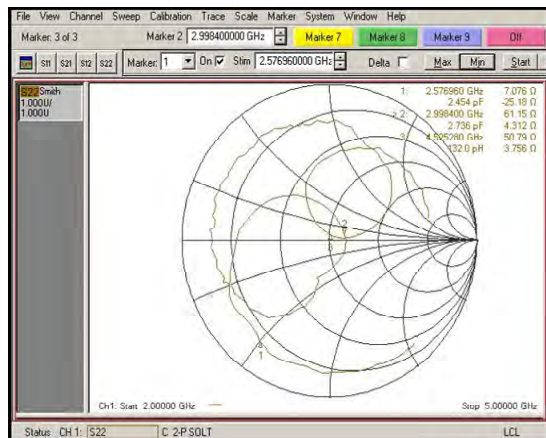
The length of the notch $L_1 = 1.0$ mm to 5 mm at fixed width = 10mm

The width of the notch $W_1 = 6$ mm to 10 mm at fixed length = 2 mm

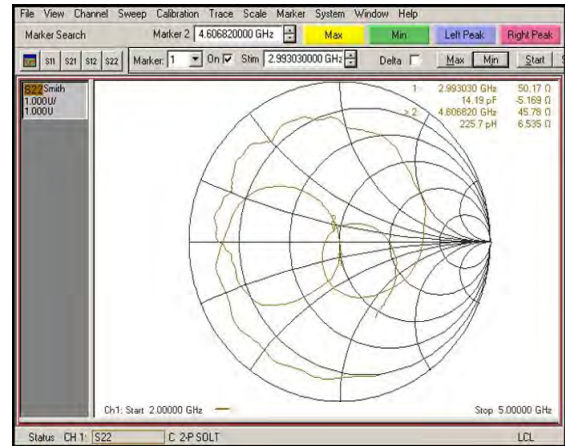
5. Discussion of Results

1) The variation of input impedance with frequency for different notch length for a given width is shown in Figures 2(a) to 2(d). It is observed that notch microstrip antenna shows dual resonance in which lower and upper resonance frequencies increases with increasing notch length from 2mm to 5mm.

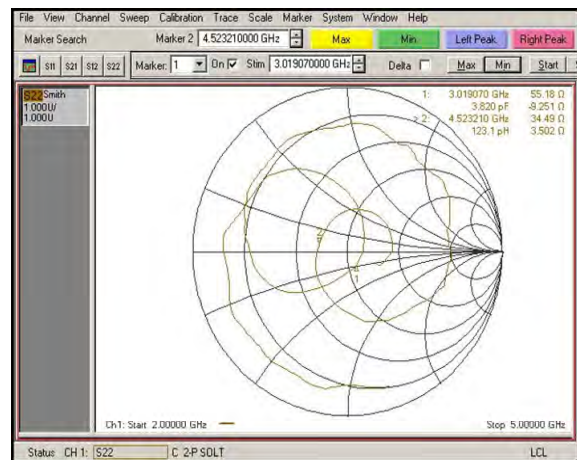
2) The variation of input impedance with frequency for different notch width for a given length is shown in Figures 3(a) to 3(d). It is observed that notch microstrip



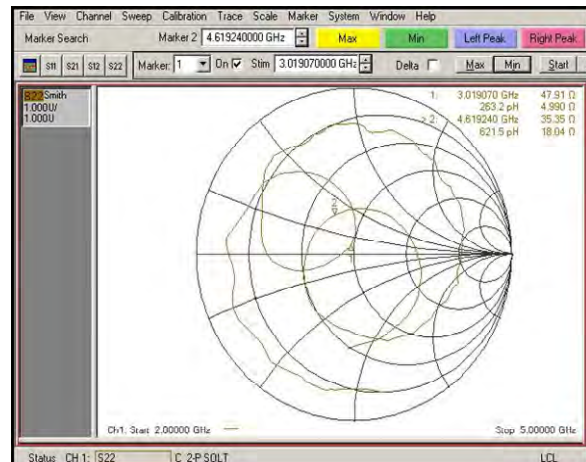
(a)



(b)



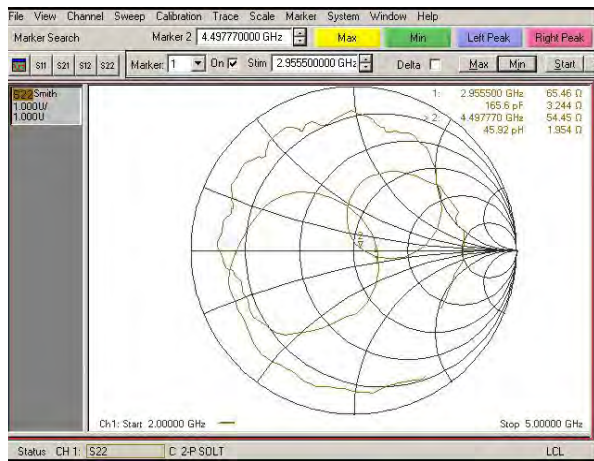
(c)



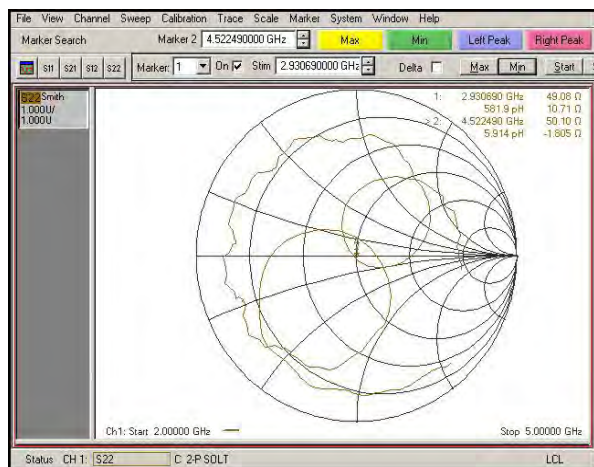
(d)

Figure 2. (a) Variations of input impedance with frequency for notch length=2mm at width =10mm; (b) Variations of input impedance with frequency for notch length=3mm at width =10mm; (c) Variations of input impedance with frequency for notch length = 4mm at width =10mm; (d) Variations of input impedance with frequency for notch length=5mm at width =10mm.

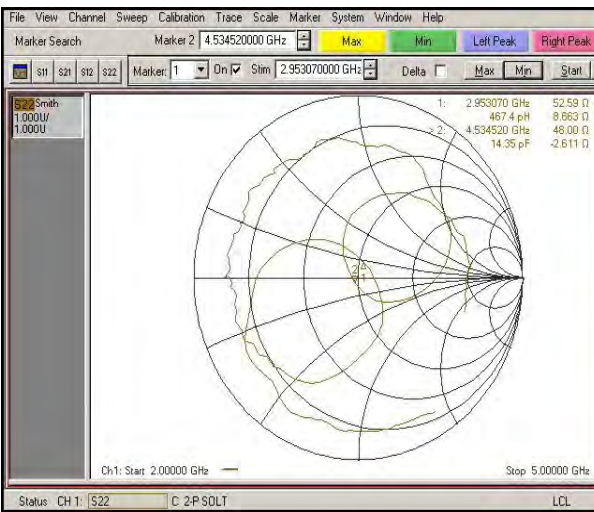
antenna shows dual resonance in which lower resonance frequency increases with increasing notch width from 6mm to 9mm, where as upper resonance is all most constant with varying notch width.



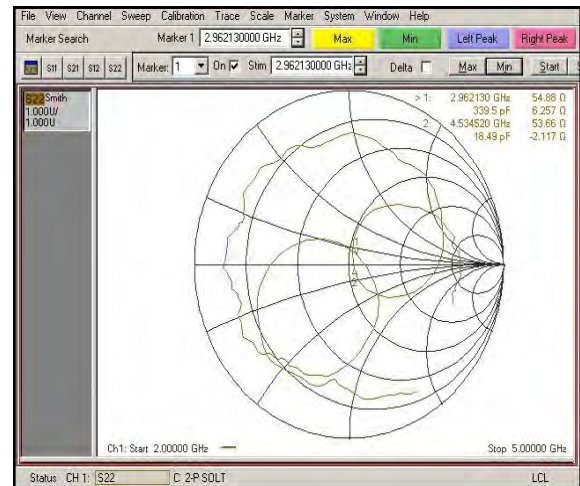
(a)



(b)



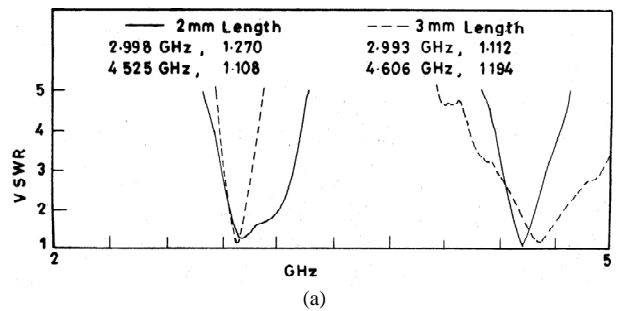
(c)



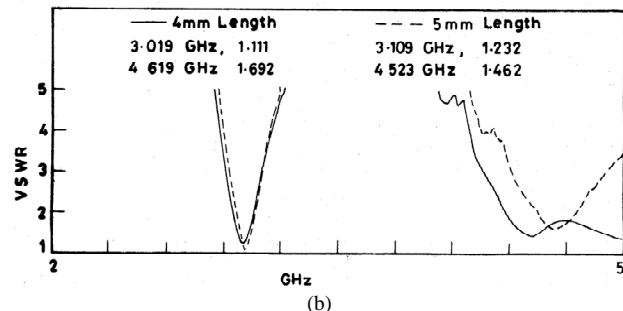
(d)

Figure 3. (a) Variations of input impedance with frequency for notch width = 6mm at length =2mm; (b) Variations of input impedance with frequency for notch width = 7mm at length =2mm; (c) Variations of input impedance with frequency for notch width = 8mm at length =2mm; (d) Variations of input impedance with frequency for notch width = 9mm at length =2mm.

3) The variation of VSWR with frequency for different notch length for a given width are shown in Figures 4(a) to 4(d) It is observed that the value of VSWR corresponding to lower resonance frequency is decreased from 1.27 to 1.11 with increasing notch length where as



(a)



(b)

Figure 4. (a) Variations of VSWR with frequency for notch length = 2 mm and 3 mm notch at width =10 mm; (b) Variations of VSWR with frequency for notch length = 4 mm and 5 mm at notch width =10 mm.

corresponding to the upper resonance frequency the value of VSWR is increased from 1.10 to 1.69.

4) The variation of VSWR with frequency for different notch width for given length are shown in Figures 5(a) to 5(d). It is observed that the value of VSWR corresponding to lower resonance frequency is decreased from 1.12 to 1.08.

5) The variation of resonance frequencies with notch dimensions is shown in the Figures 6(a) to 6(b). It is observed that both resonance frequencies are increased with notch dimensions.

6) The variation of resonance frequency ratio f_2/f_1 with notch dimensions is shown in the Figures 7(a) to 7(b). It is observed that both resonance frequencies are increases with notch dimensions.

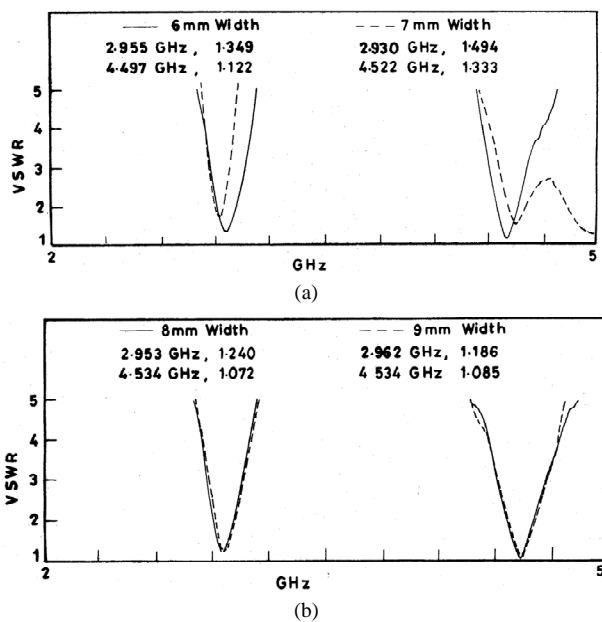


Figure 5. (a) Variations of VSWR with frequency for notch width = 6 mm and 7 mm at notch length =2 mm; (b) Variations of VSWR with frequency for notch width = 8 mm and 9 mm at notch length =2 mm.

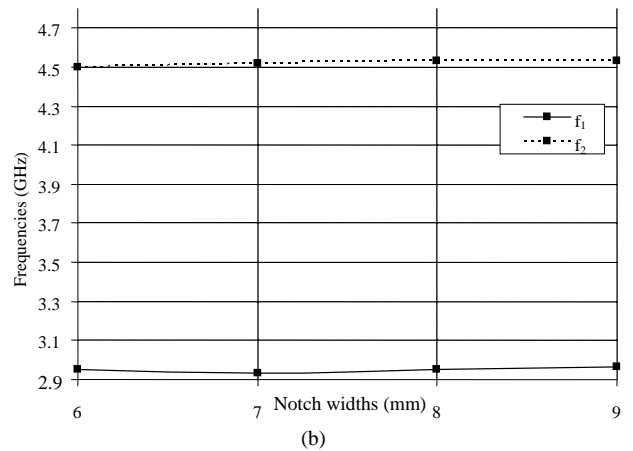
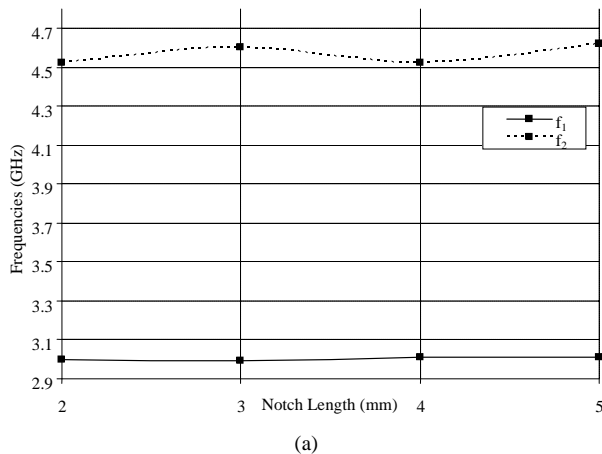


Figure 6. (a) Variations of resonance frequencies with notch lengths for a given width; (b) Variations of resonance frequencies with notch width for a given length.

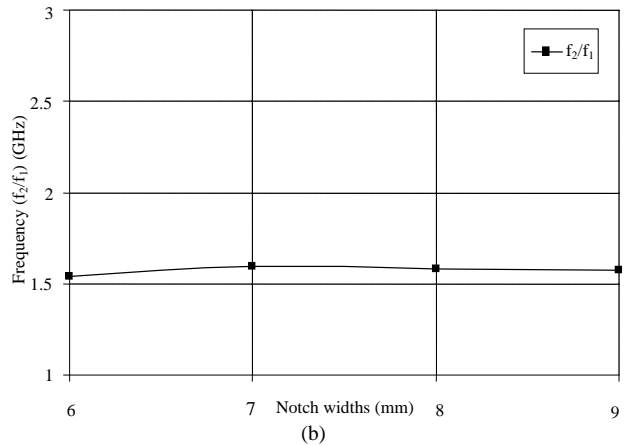
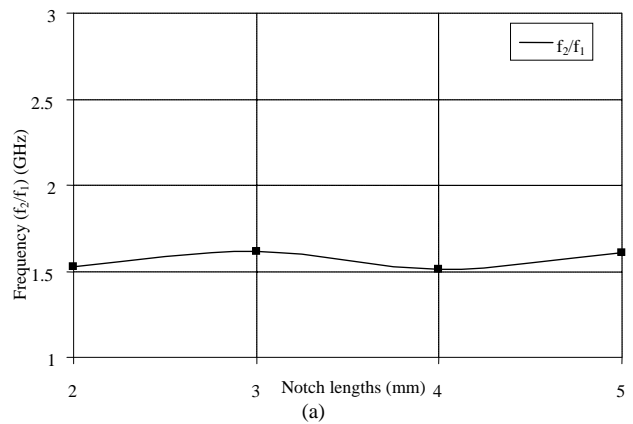


Figure 7. (a) Variation of frequency ratios (f_2/f_1) with notch length for a given width; (b) Variation of frequency ratios (f_2/f_1) with notch width for a given length.

6. Acknowledgment

The authors would like to thank Professor Arun Kumar and Shri R. K. Malaviya of the Space Application Centre, Indian Space Research Organization Ahmedabad, for

providing the measurement facilities.

7. References

- [1] I. J. Bahl and P. Bharta, *Microstrip Antenna*, Artech House, Massachusetts, USA, 1980.
- [2] S. K. Polit and A. Hamad, "Dual-band notch microstrip antenna for mobile communications," *Asia Pacific Microwave Conference Proceeding New Delhi*, Vol. 2, pp. 299–302, pp. 17–20, December 1996.
- [3] H. Nakano and K. Vichien, "Dual-frequency square patch antenna with rectangular notch," *Electronics Letters*, Vol. 25, No. 16, pp. 1067–1068, August 1989.
- [4] L. I. Basilio, A. K. Jeffery, T. Williams, and A. S. Long, "The dependence of the input impedance on feed position of probe and microstrip line fed patch antenna," *IEEE Transactions on Antennas Propagation*, Vol. AP-49, pp. 45–47 January 2001.
- [5] E. Chang, S. A. Zong, and W. F. Richards, "An experimental investigation of electrically thick rectangular microstrip antenna," *IEEE Transactions on Antennas Propagation*, Vol. AP-34, pp. 767–772, 1986.
- [6] D. M. Pozar and B. Kaufman, "Increasing the band width of a microstrip antenna by proximity coupling," *Electronics Letters*, Vol. 23, No. 8, pp. 368–369, April 1987.
- [7] H. F. Poes and A. V. V. De Capelle, "An impedance matching technique increasing the band width of microstrip antenna," *IEEE Transactions on Antenna and Propagation*, Vol. AP-37, No. 11, pp. 1345–1354, November 1989.
- [8] S. K. Palit "Broad band microstrip antenna design," *Chinese Journal of radio science*, August 1995.
- [9] C. L. Li, C. F. Wen, and Y. K. Ling, "Dual-band dipole-loaded notch antenna," *The 23rd International Technical Conference on Circuits/Systems, Computers and Communications (ITC-CSCC 2008)*, pp. No-1797–1800.
- [10] Shivnarayan and B. R. Vishvakarma, "Analysis of notch loaded patch for dual-band operation," *Indian journal of Radio and Space Physics*, Vol. 35, pp. 435–442, 2006.
- [11] J. Y. Hui, and Z. S. shi, "Notch triangular microstrip antenna for dual-frequency operation," *Journal of Shanghai University*, pp. No-375–378, 2003.
- [12] M. V. Schneider, "Microstrip lines for microwave integrated circuits," *Bell System Technology Journal*, Vol.48, pp. 1421–1444, May–June 1969.

The Quantized Characterization of Cooked Rice Hardness and Research on the Automatic Measurement Technology

Nan Jiang¹, Yuan Gao², Jiping Zhou¹, Longqin Gao¹, Jianhua Zhou¹, Qigen Dai²

¹Mechanical Engineering College, Yangzhou University, Yangzhou, China

²Agricultural College, Yangzhou University, Yangzhou, Jiangsu, China

E-mail: jpzhou@yzu.edu.cn

Received August 27, 2009; revised September 19, 2009; accepted October 4, 2009

Abstract

The hardness of cooked rice is one of the most important criteria which determine the rice quality. The commonly used near-infrared reflectance (NIR) method is still in argument due to its indirectness and possible error. In this paper, a mechanical method was proposed and its principle, automation, components and operative reliability were evaluated and compared with the NIR method. The results showed that the mechanical testing method can accurately detect the rice quality and were consistent with the NIR testing data. This new mechanical method can be effectively used in rice quality testing and branding with the advantage of simplicity, accuracy and reliability.

Keywords: Rice Hardness, Measurement System, Stress-Strain

1. Introduction

Rice is one of the most important food crops in China, and China also is the biggest country of production and consumption of rice. The people's requirement of high quality rice is increased with time [1]. The requirement of high quality rice will be substantially increasing in market demand. Therefore, the study and identification of rice eating quality will be more emphasized.

The rice hardness is one of the important factors affecting rice eating quality. The existing detection methods of rice hardness are sensory evaluation [2] and physical-chemical analysis [3]. The former has established a series of the evaluation standards, and these have some guiding effects to the rice quality testing. But it also has some uncertain factors and thus is lack of public reliability and persuasion. Researchers are searching a conformable and scientific method to test the quality of rice and other organic solids. Procter (1955) have putted forward the standard of chew food, and use the human tactility to research the physical characteristics of food [4]. Procter and Szczeniak (1963) have confirmed the Texture Profile Analysis to describe the quality of food, and use the stress-time curve to show the food quality [5]. Recent years researchers use the Texture Analyzer and Instron Universal Texting Machine to test the cooked-rice quality especially the hardness and viscosity, but the method's adaptability is few to testify. Meanwhile the Taste Ana-

lyzer has been developed to test the rice quality [6], which is based on the NIR (Near-Infrared Reflectance) technique, analyzes the rice quality components (protein, starch, oil, sugar and water etc), and finally indirectly get the appearance, hardness, viscosity, equilibrium degree and taste data of rice., This method obtains the result from conversion of a rage of experiential formulas, not through the press the rice directly to get the testing result, so its analysis result is not very precise. Besides, another technique is use the Image Reconstruction based on Analytic Method to test the brightness and glossiness of rice, to be brief is through the appearance to judge the eating quality of cooked rice [7].

Therefore, the establishment of a new method and technique to reflect accurately the rice hardness and other characteristic parameters is very important for rice grade identification and quality breeding through modern genetic engineering.

2. The Measurement and Analysis of Rice Hardness

2.1. The Rice Hardness and Stress Analysis

The rice hardness means the resistance of the cooked rice to external-introduced pressure. When people chew the rice, they can intuitively feel its hardness or softness. When the external pressure reaches a critical value, the

rice will break thoroughly, and this critical value that can be used to characterize the rice hardness is usually between 0~150g force and the strain is between 0~3mm, so the key point is to get the stress-strain relationship of the rice.

2.2. The Basic Ideas of Measurement

Now there is still not a mature and reliable method and technique for micro-stress and displacement measurement. Based on analysis of existing methods and technology of food testing [8–10], correct understanding and grasp of rice relationship between the material properties, machinery mechanics measurement techniques were used to establish a measurement of rice stress-strain, according to the characteristics of small size, displacement and force. The method developed in this study could measure the rice force which could be conversed to express the rice hardness.

2.3. The Basic Principles of Measurement

The basic principles of measurement are the double cantilevers stress and strain measurement techniques as shown in Figure 1(a). The rice to be measured is put on the pallet between the double cantilevers, external force push the indenter, which fixed on the up-cantilever, to oppress the rice, then the rice will press the down-cantilever. There are 8 resistance strain gauges (BHF350-3AA type) in Figure 1(b), and the Figure 1(c) shows that the strain gauges 1~4 are linked with differential circuit to detect the double cantilevers relative deformation that is the strain of rice; meanwhile, the strain gauges 5~8 are linked with another differential circuit to detect the force of down-cantilever that is the stress of the tested rice. Then through the data wire transfer the stress-strain signal of rice, which acquired by the data acquisition board, then analysis the data to obtain the rice hardness finally.

3. The Measurement System

Figure 2 shows the basic ideas and principles for the

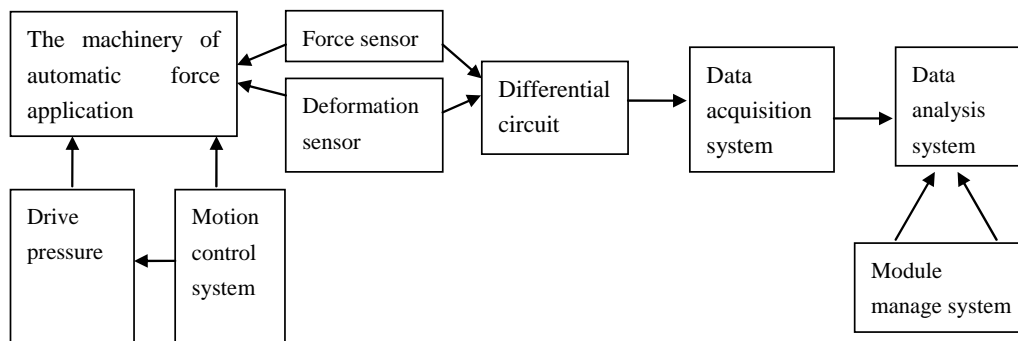


Figure 2. The components of automatic measurement system.

measurement of the rice, and the automatic system used to measure the rice hardness.

3.1 The Machinery of Automatic Force Application

The rice automatic measurement system is composed by motor, transmission shaft, cam, guide rod and spring etc. as shown in Figure 3. The principle is that when the motion control system sends a signal to the motor, the motor drives the cam to rotate through the transmission shaft, the cam presses the up-cantilever through the guide rod, meanwhile press the rice. The loading stroke decided by the size of the rice (usually is the 85% of the rice), and the maximum loading stroke is the net volume of the cam. The control program detects the deformation of the rice to judge whether it reaches the loading stroke. When the deformation reaches the stroke, the motor will stop loading and drive the cam to reverses to the initial position.

3.2. Measurement and Date Acquisition System

In order to get the measured value of micro-stress and strain of different materials, the double cantilevers' high

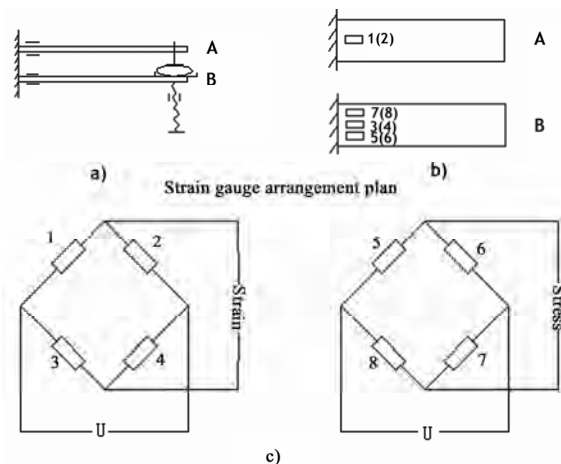


Figure 1. Schematic diagram of measurement principle.

ratio of length and width is 200:15:1 determined preliminarily. Besides, we choose the AAA resistance strain gauge, and the requirements of patch, substrate and cure are very strictly designed, and measurement accuracy is ensured by means of the differential circuit and compensation (Figure 1(c)). The deformation signals of the double cantilevers are collected by the special data acquisition board, and then through the data wire linked to the computer.

3.3. Data Analysis System

Language Delphi 7 is used to compile the program of data analysis system, draw the “stress-strain”, “stress-time” and “strain-time” curves, and to calculate the maximum stress and eigenvalue, record and save the data of the rice (Figure 4).

4. The System Operation and Test Verification

4.1. The Initialization of the Measurement System

Figure 5 shows that the automatic measurement system designed and manufactured by ourselves, composed by automatic measurement equipment, data wire and computer.

4.1.1. Stress-Strain Parameter Calibration

In order to get the relationship between stress-strain, micro-force and deformation, and to ensure the accuracy before the first time to run the system, we demarcate both force signal and strain signal. The force signal of the up-cantilever is demarcated by the spiral micrometer, it presses the up-cantilever 0.2mm each time, and the strain signal of the down-cantilever is demarcated by weights, they press the down-cantilever 10g each time. The demarcation value of force and strain signal is listed in Table 1 and Table 2. The average of the three demarcation values is used as the basis. According to the Table 1 and Table 2 the linearity of the demarcation values is good, the data acquisition system can meet the requirement.

4.1.2 System Self-Check

After demarcating, the system must self-check. According to the theory, without the test object, the double cantilevers are rigid connection, when the machinery of automatic force application press the double cantilevers the relative deformation should be zero, and the stress-strain curve is straight line of which the angle is 45° with the coordinate axis, meanwhile the curves of loading and unloading should be coincident in Figure 6 which shows that the system is accurate and reliable.

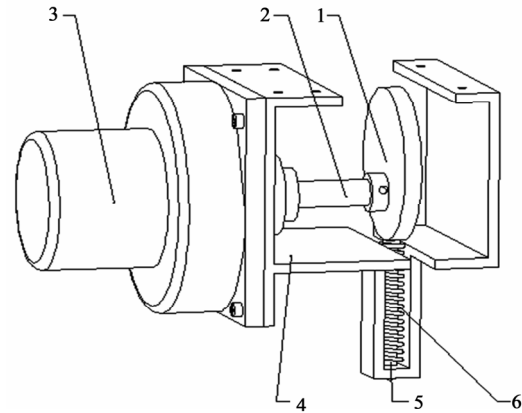
4.2. The Preparation of Test

4.2.1. Testing Scheme

According to the evaluation standard of the rice quality,

in order to verify the adaptability, reliability and accuracy of the rice hardness test system, we establish the testing scheme as follows:

Firstly, aiming at the same variety rice using the different types of indenters to test the rice, and analysis the



1.Cam 2.Transmission shaft 3.Motor
4.Box 5.Guide cod 6.Spring

Figure 3. The machinery of automatic force application.

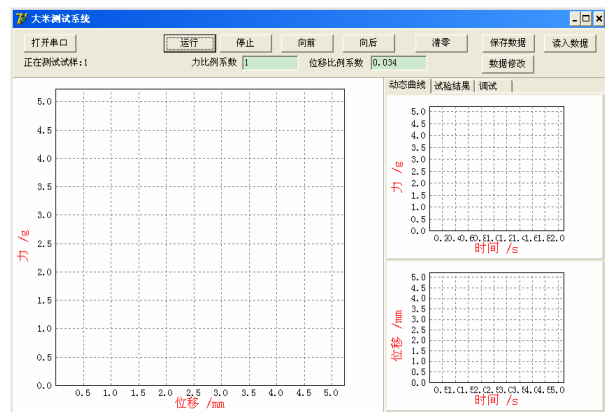


Figure 4. The interface of data analysis system.

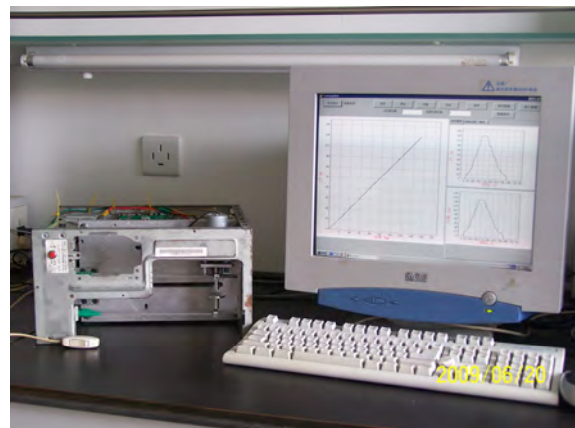


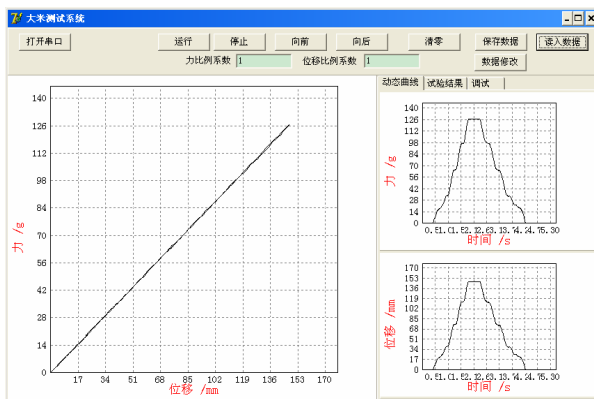
Figure 5. Automatic measurement system.

Table 1. Force demarcation.

Standard force (g)	Force signal equivalent	Standard force (g)	Force signal equivalent
0	0.0	90	1033.3
10	86.0	100	1166.7
20	255.0	110	1213.3
30	335.3	120	1350.0
40	465.7	130	1500.0
50	563.3	140	1636.7
60	686.7	150	1716.7
70	813.3	160	1843.3
80	920.0		

Table 2. Strain demarcation.

Standard strain (mm)	Strain signal equivalent	Standard strain (mm)	Strain signal equivalent
0	0.0	1.6	175.3
0.2	22.5	1.8	197.0
0.4	42.7	2.0	219.0
0.6	65.8	2.2	241.0
0.8	86.0	2.4	262.0
1.0	112.7	2.6	280.0
1.2	131.7	2.8	301.3
1.4	153.7	3.0	322.0

**Figure 6. The graph of system self-check.**

consistency of the rice under the same indenter;

Secondly, aiming at the varied rice varieties, using the same type of the indenter to test the stress-strain, and verifying if the test system can discriminate the difference of varied rice varieties;

Thirdly, using one of the indenters to test the same variety at different time, and verifying if the test system could discriminate the change of the results with different time.

We select the five rice varieties randomly, and take the average of the test results as the measured value of the rice.

4.2.2. Preparation of Need Checking Sample

1) Preparation of the test rice

According to the standard cooking method [11] to pre-

pare the test rice: 1) use the electronic balance to weigh 30g rice; 2) wash the rice four times, and add the 1.33-times water; 3) immersing the rice 30 minutes, then cooking 30 minutes; 4) after the rice cooked standing it 10 minutes, then cooling it 20 minutes in the cooling equipment; 5) extract the sample to test during which the sample is stirred to maintain uniformly.

2) Preparation of the indenters

For the requirement of the test, at the beginning of the scheme establishment we use the different indenters to test the rice hardness, in order to get the suitable one. We prepare the $\Phi 2\text{mm}$ and $\Phi 3\text{mm}$ spherical indenter, $\Phi 2\text{mm}$ and $\Phi 3\text{mm}$ plane indenter, $\Phi 10\text{mm}$ and $\Phi 15\text{mm}$ cylindrical indenter, $10\text{mm} \times 1\text{mm}$ tool form indenter, respectively, while the cylindrical indenter is used to test the rice-flour dough mainly.

4.3 Measurement Results and Analysis

1) Choose the first class rice (according to National Standard), and use the different indenters to test it, the measured results are showed in Table 3. We can educe that the stresses are different with the different indenters, and the average stresses exhibit a obvious difference. But the slope of the stress-strain curves has a good consistency. Therefore, we could use the slope to express the hardness of the cooked rice, and the big slope indicates a high hardness.

Note: the average is the ratio of maximum force to area of the indenter

2) Table 4 shows data of using the $\Phi 3\text{mm}$ plane indenter to test the first class rice and the data of Baoying lake organic rice at the different time is also listed in Table 4. The all listed results show that the testing system can distinguish the difference of the hardness of the rice at the different time.

3) Table 5 shows data of using the $\Phi 10\text{mm}$ cylindrical indenter to test the six different breed rices. We can see that the testing system could distinguish the variance of the rice hardness.

4) Comparison with the Japanese taste analyzer

According to the test results of hardness which is tested through the Taste Analyzer STA 1A indirectly, we use the rice under the same cooking standard to test, the results are in Table 5. The hardness of the same variety exhibits the consistency between the automatic testing system and the Japanese taste analyzer, which prove the correctness of the system.

5) Analysis of system measuring error

According to the test scheme, every variety repeats 5 times. Take the first class rice as example, use the $\Phi 3\text{mm}$ plane indenter to test, under the cooking standard the test values are in Table 7. The absolute error is 0.2691, and the average of the relative error is 1.35%, which shows that the error and the reproducibility of the measuring system can meet the test requirement.

Table 3. The data of the same breed rice with different pressure head.

Indenter	The maximum force (g)	Average (g/mm ²)	The slope of the curve
Φ3 plane indenter	41.2224	5.4990	19.9910
Φ3 spherical indenter	39.7255	5.3949	19.4340
Φ2 plane indenter	38.6891	13.1215	19.8397
Φ2 spherical indenter	37.3744	12.7033	19.7861
Tool form on lateral	37.4714	17.0325	19.8395
Tool form on vertical	38.1325	4.4340	19.4976

Table 4. The data of the same rice variety at different time.

Time	First class according rice	Baoying lake organic rice
0 hour	19.7433	20.7861
1 hour	19.7503	21.1354
2 hour	19.9474	21.4977
6 hour	20.3053	21.8576

Table 5. The data of contrast experiment.

Rice breed	Auto-test system	Taste analyzer
	The slope	Hardness
Daoya rice	21.5191	8.1
Baoying lake organic rice	21.0686	7.9
San'an rice	20.9645	7.6
Yueguang rice	20.8404	6.8
Xinxie rice	20.3684	6.5
The first class rice	20.3248	6.3

Table 7. The data of error analysis.

No.	1	2	3	4	5	Average
Test values	19.7433	19.9509	19.9876	20.0124	19.9473	19.9283
Absolute error		0.2691				
			Relative error			1.35%

5. Conclusions

A mechanical automatic testing system is established to quantitatively characterize the rice quality such as its hardness. Through test the deformation of the rice, we can use the slope of the curve to express the rice hardness as the evaluation standard of the rice. The test results show that the automatic testing system could detect the hardness difference of varied rice varieties, and it also could detect the change of one variety hardness with time, the testing errors and reproducibility are in accordance with the demand of the rice identification. The test results are in consistent with that of the Taste Analyzer.

This automatic testing method based on mechanical theory is feasible, it can provides a convenient, accurate and reliable method to quantitatively obtain the rice parameters, and is important for studying and characteriz-

ing the quality of organic solid substance. Further improvements are still needed in testing precision, reducing testing error, and using in other parameter measurement of rice.

6. Acknowledgement

This research is supported by the National Technology R&D Program of China (Contract No. 2006BAD02A03)

7. References

- [1] J. D. Jin and S. Y. Zhang, "Quality traits of high-quality rice at home and abroad research (in Chinese)," Chinese Journal of Jilin Agricultural Sciences, Vol. 28, No. 6, pp.13–15, 2003.
- [2] W. Y. Fu and Y. W. Xing, "Grain quality evaluation of

- current situation and prospect (in Chinese)," Chinese Journal of Natural Science Journal of Hainan University, Vol. 14, No. 3, pp. 269~271, September 1996.
- [3] X. M. Zhang, Y. C. Wang etc, "Rice taste evaluation of the progress (in Chinese)," Chinese Journal of Seed, Vol. 1, pp. 52-53, 2002.
- [4] B. E. Procter, "Instrument evaluation and initial test," Chinese Journal of Food Technology, Vol. 9, pp. 417-441, 1955.
- [5] A. S. "Szczeniak objective measurements of food texture," Chinese Journal of Food Science, Vol. 28, pp. 420-441, 1963.
- [6] X. M. Zhan, T. S. Zheng, and J. H. Tao, "Study on application of texture analyzer in quality evaluation of rice (in Chinese)," Chinese Journal of Food Science, Vol. 28, No. 9, pp. 62-65. 2007.
- [7] A. H. Cheng, X. H. Li, X. M. Yao etc, "Study on the correlation between image analysis properties and rice sensory evaluation of japonica rice in northeast china (in Chinese)," Chinese Journal of Grain and Oil Food, Vol. 14, No. 4, pp. 25-27, 2006.
- [8] X. F. Guo and Y. D. Mu, "Evaluation of a method for determining texture characteristics of cooked rice (in Chinese)," Chinese Journal, Journal of the Chinese cereals and oils association, Vol. 4, No. 21, pp. 9-11, 2006.
- [9] Y. Lan, O. R. Kunze, "Fissure resistance of rice varieties," Chinese Journal Applied Engineering in Agriculture, Vol. 12, No. 3, pp. 365-368, 1996.
- [10] Y. Lan and O. R. Kunze, "Fissure characteristics related to moisture adsorption stresses in rice," Chinese Journal Transactions of the ASAE, Vol. 39, No. 6, pp. 2168-2174, 1996.
- [11] "People's Republic of China national standard quality assessment tests of rice cooking," GB/T 15682, 1995.

Analytic Computation Method of the Equivalent Thickness of Superposition Multi-Throttle-Slices of Twin-Tubes Shock Absorber

Changcheng Zhou, Yingzi Xu

School of Transport and Vehicle Engineering, Shandong University of Technology, Zibo, China

E-mail: greatwall@sdut.edu.cn

Received August 27, 2009; revised September 22, 2009; accepted October 4, 2009

Abstract

By elastic mechanics, the deformation of single throttle-slice for shock absorber was analyzed, the formula of its deformation was established. According to the relation of the deformation of multi-throttle-slices with the pressure on each slice, the analytic formula of equivalent thickness of multi-throttle-slices was established. Followed is a practical example for the computation of the equivalent thickness of multi-throttle-slices, compared the computed results with that simulated by ANSYS. The results show that the computation method of equivalent thickness of multi-throttle-slices is accurate enough.

Keywords: Twin-Tubes Shock Absorber, Multi-Throttle-Slices, Equivalent Thickness, Analytic Computation

1. Introduction

With the improvement of automobile technology, the velocity also improves, and there is a higher request to the smoothness and the security [1,2]. The characteristic of shock absorber influences driving smoothness and security of vehicles, nevertheless, it depends on the quality of the design and manufacture of shock absorber [3]. The telescopic twin-tubes shock absorber is widely used for vehicles. Nevertheless, it is still a puzzling problem for the throttle valves parameters design to calculate accurately the equivalent thickness of multi-throttle-slices. At present, both in domestic and abroad, in despite of many scholars analyzed the computation of equivalent thickness of multi-throttle-slices mostly by the finite element methods, they given out some qualitative conclusions only. This situation is un-accommodated to highly developed technology of automobile and affects the design quality of shock absorber. For the parameters design of throttle valves, there is not any analytic method yet, only with the experience of designer, testing and modification repeatedly [4,5]. It is said that the design for parameters of multi-throttle-slices, firstly a parameter value is guesstimated on experience, then testing and modification time and again; at lastly, the design value is fixed. While one parameter changing, other parameters would also change. Therefore, this method is inaccurate, the parameters of multi-throttle-slices could not be designed reliably. The traditional method of the equivalent-thickness of multi-th-

rottle-slices is only a numerical simulation value [6,7], but it is unable to offer an analytic formula used to design the parameters of multi-throttle-slices.

In this paper, the analytic computation method of equivalent thickness of multi-throttle-slices was researched, the formula of equivalent thickness was established, and the results computed were tested with software ANSYS.

2. Deformation of Single Throttle-Slice

2.1. Mechanics Model of Single Throttle-Slice

Figure 1 is the mechanics model of elastic throttle slice. The boundary conditions of throttle slice are fixation restriction at the inner radius, and free restriction at the outer radius.

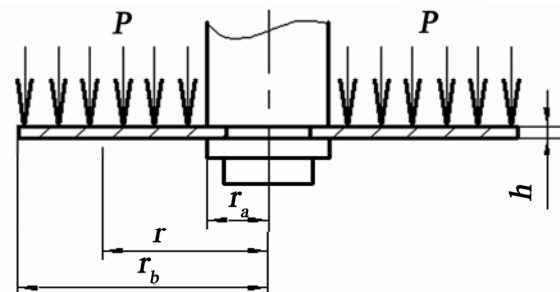


Figure 1. Mechanics model of elastic throttle-slice.

where, r_a is the inner radius, r_b is the outer radius, h is the thickness, p is the pressure, and f_r is the deformation at radius r .

2.2. Math Model of Throttle-Slice Deformation

Being symmetrical about the z -axis, the load and the structure, according to the basic principles in the elastic mechanics, the differential equation of elastic throttle slice deformation [8] is established as

$$D\left(\frac{d^2}{dr^2} + \frac{1}{r} \frac{d}{dr}\right)\left(\frac{d^2 f_r}{dr^2} + \frac{1}{r} \frac{d f_r}{dr}\right) = p \quad (1)$$

where, $D = Eh^3 / [12(1-\mu^2)]$; r is the any radius of throttle slice, $r \in [r_a, r_b]$; E is the elasticity coefficient of material of throttle slice; μ is Poisson rate; h is the thickness of throttle slice. So, the solution of (1) is as

$$f_r = C_1 \ln r + C_2 r^2 \ln r + C_3 r^2 + C_4 + \frac{3(1-\mu^2)r^4 p}{16Eh^3} \quad (2)$$

where, C_1, C_2, C_3, C_4 could be defined by the boundary conditions of throttle slice.

Therefore, analyzed the solution of the differential equation of slice deformation, the each items of it has the common factor of p/h^3 that can be bringing forward from (2), and then the deformation of throttle slice at any radius r can be obtained.

$$f_r = [K_{C1} \ln r + K_{C2} r^2 \ln r + K_{C3} r^2 + K_{C4} + \frac{3(1-\mu)r^4}{16E}] \frac{p}{h^3} \quad (3)$$

where, K_{C1}, K_{C2}, K_{C3} and K_{C4} are the residual parameters after the common factor p/h^3 is binging forward respectively from C_1, C_2, C_3 and C_4 .

2.3. Formula of Throttle-Slice Deformation

Define G_r as the deformation coefficient of throttle slice, it is as follow [9,10]

$$K_{C1} \ln r + K_{C2} r^2 \ln r + K_{C3} r^2 + K_{C4} + \frac{3(1-\mu)r^4}{16E} = G_r \quad (4)$$

The G_r is the inherent characteristic of throttle-slice deformation at radius r , denoting the deformation capability of throttle-slices.

So, the analytic formula of throttle-slice deformation at any radius was written briefly as

$$f_r = G_r \frac{p}{h^3} \quad (5)$$

For example, one throttle slice's G_r is shown as in Figure 2.

3. Equivalent Thickness of Multi-Throttle-Slices Superposition

3.1. Model of Multi-Slices Equivalent Thickness

The sketch of the equivalent thickness of multi-throttle-

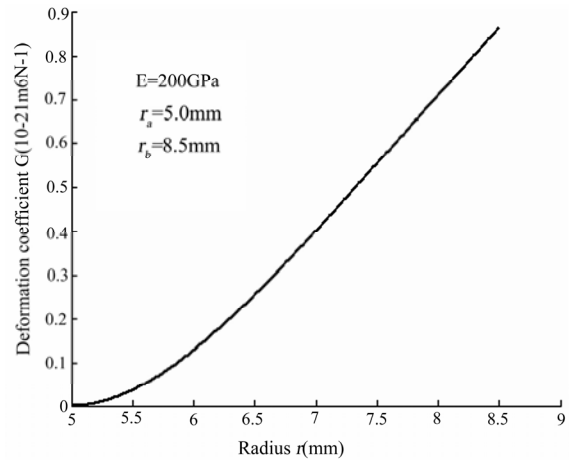


Figure 2. Curve of throttle slice deformation coefficient vs. radius.

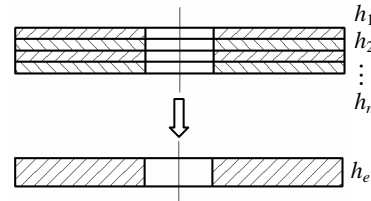


Figure 3. Sketch of multi-throttle-slices superposition.

slices superposition is shown in Figure 3.

3.2. Formula of Multi-Slices Equivalent Thickness

The model of throttle-slices superposition with unequal thickness could be taken as the paralleled springs that have the equal length, unequal elasticity coefficient.

The deformations of multi-slices are equal under same pressure. According to (5), it can be obtained such as

$$G_r \frac{p_1}{h_1^3} = G_r \frac{p_2}{h_2^3} = \dots = G_r \frac{p_n}{h_n^3} = G_r \frac{p}{h_e^3} \quad (6)$$

The forces on multi-slices are unequal, but the summation of theirs is equal to the total force, i.e. $p_1 + p_2 + \dots + p_n = p$.

Form (19), the equivalent thickness h_e is written as

$$h_e = \sqrt[3]{h_1^3 + h_2^3 + \dots + h_n^3} \quad (7)$$

If the each slice of multi-throttle-slices has multi-group thickness, i.e. $h_1, n_2; h_2, n_2; \dots h_n, n_n$, so, (7) can be expressed

$$h_e = \sqrt[3]{n_1 h_1^3 + n_2 h_2^3 + \dots + n_n h_n^3} \quad (8)$$

If the thickness of multi-throttle-slices is be equal each other, i.e. $h_1=h_2 \dots =h_n$, thus (7) can be written as

$$h_e = h_1 \sqrt[3]{n} \quad (9)$$

3.3. Equivalent Computation of Multi-Slices

According to (7), the equivalent thickness of multi-slices can be computed, and the curve of equivalent thickness vs. slices number was shown as in Figure 4.

From (8) and Figure 4, it is known that the relations of the thickness of multi-slices with the equivalent thickness are as follows

- 1) The three power of the equivalent thickness is the sum of three power of each slice thickness.
- 2) The equivalent thickness of unequal thickness multi-slices is larger than the maximum thickness, i.e. $h_e > \max[h_i]$.
- 3) The thickness of throttle-slice is standard, so, adapted to batch manufacture, and price depressed.

4. Deformation of Multi-Throttle-Slices

4.1. Deformation

For multi-throttle-slices h_1, h_2, \dots, h_n , the equivalent

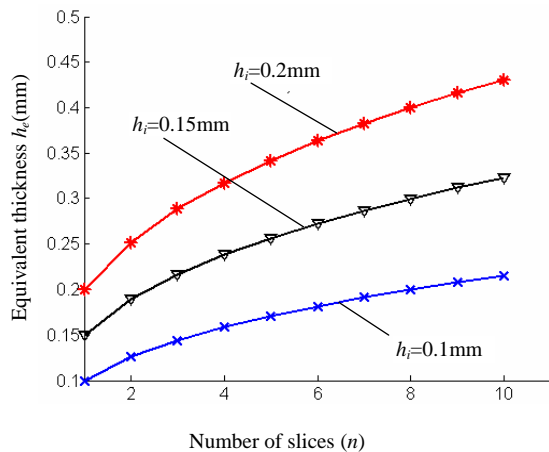


Figure 4. Curves of equivalent thickness at different slices number.

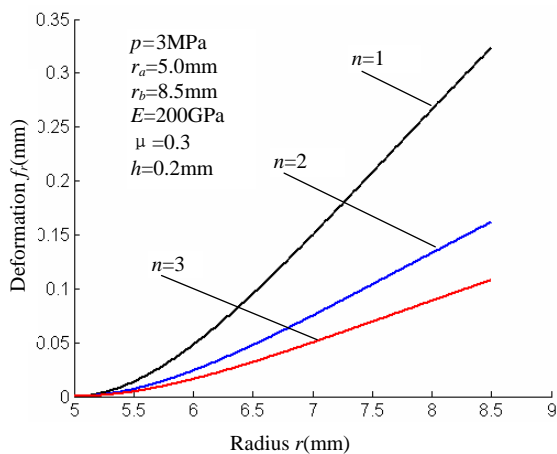


Figure 5. Deformation curve of multi-throttle slices superposition.

thickness of them is h_e , the pressure loaded on multi-throttle-slices is p . The deformation of multi-throttle-slices could be regarded as the deformation of the single slice of thickness h_e .

According to (5), the deformation of multi-throttle-slices can be expressed as

$$f_r = G_r \frac{p}{h_e} \tag{10}$$

Combining (10) with (7), so (10) is written as

$$f_r = G_r \frac{p}{h_1^3 + h_2^3 + \dots + h_n^3} \tag{11}$$

From (11), it is known that the deformation of multi-slices is equal, as long as with different composing, but with the same equivalent thickness.

4.2. Computation Example

For example, if one single slice's thickness h is 0.3mm, the multi-slices $h_1=0.2\text{mm}$, $n_1=3$ and $h_2=0.1\text{mm}$, $n_2=3$, the equivalent thickness h_e is 0.3mm, the pressure $p=3\text{MPa}$. From (11), the deformation of multi-throttle-slices is equal to that of single slice of thickness h_e .

For the multi-slices with different thickness, whereas the pressure is same, their deformation would be different. For example, the deformations computed by analytic formula of multi-slices with different equivalent thickness are as shown in Figure 5.

The computed deformation of throttle-slice is shown as in Table 1.

5. Simulation Certification

The throttle slice model can be established with the finite element method by numeral software ANSYS, meshing with 0.1mm, loading and simulating.

The physical parameters of single throttle slice is as above, $h=0.3\text{mm}$; and the multi-slices is $h_1=0.2\text{mm}$, $n_1=3$ and $h_2=0.1\text{mm}$, $n_2=3$, the equivalent h_e is 0.3mm. Under pressure 3MPa, the simulated results of deformation of single slice and multi-slices are as shown in Figure 6, and Figure 7, respectively.

From Figure 6, it is known that the maximum deformation simulated of single-slices is 0.126mm.

Compared with Table 1, the maximum deformation of single slice computed is very close to that simulated of multi-throttle-slices superposition, and their tolerance is only 0.03mm. It is shown that the computation method of single slice's deformation is accurate enough.

Table 1. Deformation of multi-throttle-slices at different radius r .

Radius (mm)	5.0	6.0	7.0	8.0	8.5
Coefficient ($10^{-22}\text{m}^6/\text{N}$)	0.000	1.350	4.207	7.467	0.909
Deformation (mm)	0.000	0.014	0.044	0.078	0.096

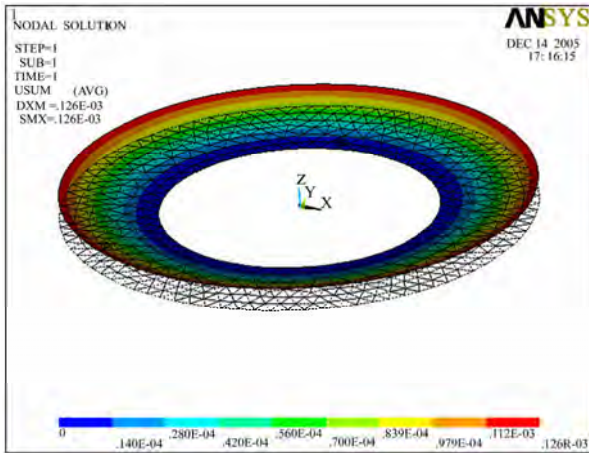


Figure 6. Deformation map simulated of single-throttle slices.

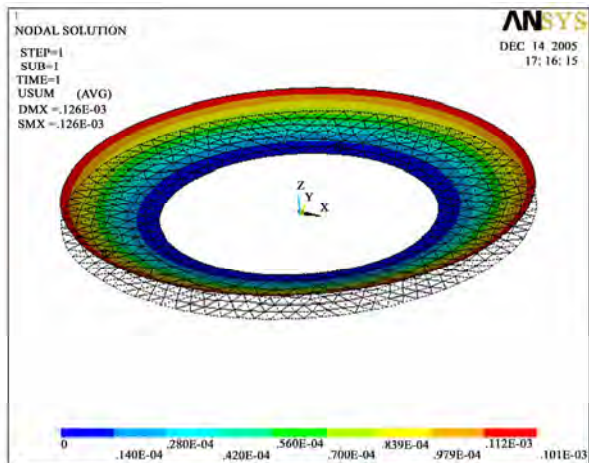


Figure 7. Deformation map simulated of multi-throttle-slices superposed.

From Figure 7, it is known that the maximum deformation simulated of multi-throttle-slices is 0.101mm respectively.

Compared with Table 1, the maximum deformation computed of multi-throttle-slices superposition is close to that simulated, the tolerance is only 0.005mm. It is shown that the computation method of the equivalent thickness of multi-throttle slices superposition is accurate enough.

6. Conclusions

By the analytic computation and simulation certification to the equivalent thickness of multi-throttle-slices, it is known that the analytic formula of equivalent thickness of multi-throttle slices is accurate, simple and applied.

With it, the equivalent thickness of multi-throttle-slices with different thickness can be computed accurately.

The deformation computed of multi-slices is close to that simulated by ANSYS. It is shown that the computation method of the equivalent thickness of multi-throttle-slices is accurate enough, can be used to design the parameters of throttle-slices of shock absorber.

7. Acknowledgment

The authors thank the Nature Science Foundation of Shandong (No. Y2007F72) for the funding support.

8. References

- [1] D. F. Yu and Q. H. Chen, "Design study of smoothness-to-safety ratio in suspension shock absorber outer characteristic," *Acta Armamentarii: The Volume of Tank, Armored Vehicle and Engine*, Vol. 87, No. 3, pp. 11–17, 2002.
- [2] C. C. Zhou, Z. Y. Zheng, and X. Y. Zhang, "Design method for throttle holes area of telescopic shock absorber for small electric vehicles," *Journal of Asian Electric Vehicles*, Vol. 7, No. 1, pp. 1191–1197, 2009.
- [3] X. M. Fen and Z. M. Liu, "Development and current situation of automobile hydraulic telescopic damper technology," *Journal of Wuhan University of Science and Technology*, Vol. No. 8, pp. 340–343, 2003.
- [4] T. Ashida, D. Tanaka and S. Minami, "A method to determine the velocity profiles from the power consumption of electric vehicles," *Journal of Asian Electric Vehicles*, Vol. 5, No. 2, pp. 1027–1032, 2007.
- [5] S. Matsugaura, H. Nishimura, M. Omae, *et al*, "Development of a driver-monitoring vehicle based on an ultra small electric vehicle," *Journal of Asian Electric Vehicles*, Vol. 3, No. 2, pp. 758–762, 2005.
- [6] S. M. Li, Z. H. Lü, "Technology development of cylindrical fluid drag shock absorber for motor vehicle," *Automobile Technology*, Vol. 32, No. 8, pp. 10–16, 2001.
- [7] Y. Chen, H. E. Hui and J. F. Bai, "Analysis of hydraulic shock absorber spring valve chip deformation of charade car," *Automobile Technology*, Vol. 31, No. 1, pp. 19–21, 2000.
- [8] Z. L. Xu, "Elasticity mechanics," Beijing: Higher Education Press, 2001.
- [9] C. C. Zhou, L. Gu, and L. Wang, "Bending deformation and coefficient of throttle-slice," *Transactions of Beijing Institute of Technology*, Vol. 26, No. 7, pp. 581–584, 2006.
- [10] C. C. Zhou and L. Gu, "Superposition throttle slices opening size and characteristic test of telescopic damper," *Chinese Journal of Mechanical Engineering*, Vol. 43, No. 6, pp. 210–215, 2007.

Sliding Mode Control with Auto-Tuning Law for Maglev System

Lingling Zhang¹, Zhizhou Zhang^{2*}, Zhiqiang Long², Aming Hao²

¹College of Mathematics and Econometrics, Hunan University, Changsha, China

²College of Mechatronics Engineering and Automation, National University of Defense Technology, Changsha, China

E-mail: zzz336@126.com

Received September 5, 2009; revised September 27, 2009; accepted October 4, 2009

Abstract

This paper presents a control strategy for maglev system based on the sliding mode controller with auto-tuning law. The designed adaptive controller will replace the conventional sliding mode control (SMC) to eliminate the chattering resulting from the SMC. The stability of maglev system is ensured based on the Lyapunov theory. Simulation results verify the effectiveness of the proposed method. In addition, the advantages of the proposed controller are indicated in comparison with a traditional sliding mode controller.

Keywords: Sliding Mode Control, Maglev System, Lyapunov Theory, Auto-Tuning

1. Introduction

Maglev (Magnetic Levitation) train is a late-model railway vehicle with many good performances such as high speed, comfort, low environmental pollution, low energy consumption and so on. Lots of countries have started up the engineering study of maglev train [1,2].

The dynamic response of vehicle/guideway system affects the running safety, ride comfort and system costs heavily, which are crucial factors for maglev train commercial application [3,4]. Due to open-loop instability and inherent nonlinearities associated with a voltage-controlled magnetic levitation system, a feedback control is necessary to achieve a stable operation. Recently, quite a few control strategies have been developed and applied widely in the industrial field of maglev technology, such as bang-bang control [5], adaptive non-smooth control [6], hybrid control [7] and H_∞ control method [8], etc.

Sliding mode control is a powerful robust approach for controlling the nonlinear dynamic systems [9]. The advantage of sliding mode control is robustness against parameter matched uncertainties and external disturbance and so on. In general, vehicle-guide vibration of maglev system is easily subjected to external disturbance. Even though the approach of sliding mode control is one of potential control candidates for maglev system, it has some limitations such as discontinuous control law and

chattering action, which lead to the appearance of input chattering, the high-frequency plant dynamics and unforeseen instability in real application. In order to alleviate the high-frequency chattering, control researchers have proposed many strategies, such as the boundary layer technique [10,11] and parameter identification mechanism with self-tuning [12,13]. In [14–16], using a modified hyperbolic tangent function as the activation function, the laws for tuning boundary layer thickness and control gain were proposed.

In this paper, the sliding mode control technique with auto-tuning law is applied to a voltage-controlled magnetic levitation system. The task of the control system is to dynamically regulate control voltage which drives the magnet to adjust the magnetic force to maintain a desired gap. Firstly, to simplify the mathematical model of maglev system, we discuss a 4-D maglev system via alternating physical variables of maglev system. In the following, with regard to this maglev system, four error variables are chosen to define the switching surface, and then a traditional sliding mode controller is designed accordingly [17]. In order to eliminate high-frequency control and chattering around the sliding surface, an auto-tuning neuron is introduced as an adaptive controller to guarantee the convergence of all states for maglev system. Simulations results show the control performance of our proposed method.

The paper is organized as follows: In Section 2, we give a mathematical model of maglev system, and then choose four error variables to determine the sliding surface. In Section 3, we design a general sliding mode controller and a systematic sliding mode controller with self-tuning law respectively. Simulation results will be given to validate the effectiveness of our proposed controller in Section 4. Conclusions are drawn in Section 5.

2. Sliding Surface Design of the Maglev System

The maglev system is a complicated system with machinery, controlling and electromagnetic elements integrated together. Figure 1 shows its working elements.

According to [3], m denotes the weight of the electromagnet; and z represents the absolute displacement of the electromagnet in the vertical. R is the resistance of the electromagnet. I and $V(t)$ are current and voltage of the electromagnet winding, respectively. The control current I is driven by control voltage $V(t)$ to maintain the air gap z at its nominal value. Define $y = [y_1, y_2, y_3]^T = [z, \dot{z}, I]^T$, then dynamical and electromagnetic equations of the system are given as

$$\begin{aligned} \dot{y}_1 &= y_2, \\ \dot{y}_2 &= g - \frac{k y_3^2}{m y_1^2}, \\ \dot{y}_3 &= \frac{y_2 y_3}{y_1} - \frac{R y_1 y_3}{2k} + \frac{y_1}{2k} V. \end{aligned} \tag{1}$$

where $k = \frac{1}{4} \mu_0 N^2 S_0$, μ_0 is the magnetic permeability in vacuum, N is the number of turns of coil, and S_0 is the effective pole area of electromagnet.

Note that this electromagnetic suspension system is unstable without control voltage V . In closed-loop system, gap sensor measures the relative interval between electromagnet and guideway while accelerometer measures the absolute kinetic acceleration of the electromagnet. Based on feedback signals from sensors, the controller can generate certain control voltage according to control algorithm. With the calculated control voltage, the electromagnet can produce suitable electromagnetic force to keep itself suspending under the guideway stably.

In order to simplify the original nonlinear system (1), we choose the variable

$X^* = [x_1^*, x_2^*, x_3^*, x_4^*]^T = [z, \dot{z}, I/Z, (I/Z)']^T = [y_1, y_2, y_3/y_1, (y_3/y_1)']^T$, x_3^* represents electromotive force of the electromagnet winding which has actual physical meanings. Then the model (1) can be transformed as following:

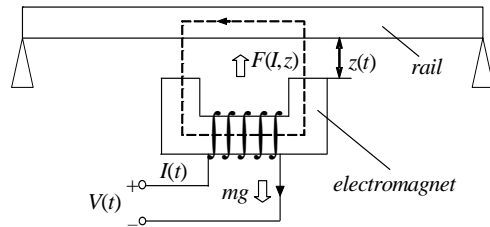


Figure 1. Structure of the maglev system.

$$\begin{aligned} \dot{x}_1^* &= x_2^*, \\ \dot{x}_2^* &= g - \frac{k x_3^{*2}}{m}, \\ \dot{x}_3^* &= x_4^*, \\ \dot{x}_4^* &= -\frac{R}{2k} (x_1^* x_4^* + x_2^* x_3^*) + \frac{1}{2k} V', \end{aligned} \tag{2}$$

where $V' = V(x_1^*, x_2^*, x_3^*, x_4^*)$ is the derivatives of $V(x_1^*, x_2^*, x_3^*, x_4^*)$. And the values of the state variables at the balance point are $X_0^* = [z_0, 0, \sqrt{mg/k}, 0]$, where z_0 is a nominal value of the air gap z .

Moving the equilibrium to the origin, letting $X = [x_1, x_2, x_3, x_4]^T$, where $x_1 = x_1^* - z_0$, $x_2 = x_2^*$,

$x_3 = x_3^* - \sqrt{mg/k}$, $x_4 = x_4^*$, (2) becomes

$$\begin{aligned} \dot{x}_1 &= x_2, \\ \dot{x}_2 &= -\frac{k x_3^2}{m} - 2\sqrt{kg/m} x_3, \\ \dot{x}_3 &= x_4^*, \\ \dot{x}_4 &= -\frac{R}{2k} ((x_1 + z_0)x_4 + (x_3 + \sqrt{mg/k})x_2) + \frac{1}{2k} U \end{aligned} \tag{3}$$

where

$$\begin{aligned} U(x_1, x_2, x_3, x_4) &= V'(x_1^*, x_2^*, x_3^*, x_4^*) = \\ &= V'(x_1 + z_0, x_2, x_3 + \sqrt{mg/k}, x_4) \end{aligned}$$

The system output is $Y = [1, 0, 0, 0]X = x_1$. For convenience, denote $f_1 = -\frac{k x_3^2}{m} - 2\sqrt{\frac{k g}{m}} x_3$,

$$f_2 = -\frac{R}{2k} ((x_1 + z_0)x_4 + (x_3 + \sqrt{mg/k})x_2).$$

Even now, a control scheme is presented to stabilize the states of maglev system. Our control objective is to stabilize all states of (3) to zero, that is to design control input to maintain the air gap z at its nominal value.

Similar to linear system, the sliding mode control of nonlinear system consists two relatively independent parts: firstly confirm that the motion on the sliding surface is globally stable, and then design a sliding control-

ler which causes the trajectories of the system to reach the sliding surface in finite time.

Denote the error variables as

$$\begin{aligned} e_1 &= x_1, \\ e_2 &= x_2, \\ e_3 &= f_1 = -\frac{kx_3^2}{m} - 2\sqrt{\frac{kg}{m}}x_3, \\ e_4 &= \dot{f}_1 = -2\left(\frac{kx_3}{m} + \sqrt{\frac{kg}{m}}\right)x_4. \end{aligned} \tag{4}$$

Then a switching surface is defined as $s=c_1e_1+c_2e_2+c_3e_3+e_4$, where c_1, c_2, c_3 are selected to be positive constant numbers such that the polynomial $\lambda^3+c_3\lambda^2+c_2\lambda+c_1$ is Hurwitz. The error dynamics in sliding mode are thus asymptotically stable.

The second step is to design a sliding controller such that the sliding surface approaches 0. And the control input U can be formulated as

$$\begin{aligned} U &= -\left[\frac{1}{2k} \frac{\partial f_1}{\partial f_3}\right]^{-1} \left\{c_1x_2 + c_2f_1 + c_3 \frac{\partial f_1}{\partial f_3}x_4 + \right. \\ &\quad \left. \frac{d}{dt}\left[\frac{\partial f_1}{\partial f_3}\right]x_4 + \frac{\partial f_1}{\partial f_3}x_2 + \beta \text{sign}(s)\right\} \end{aligned} \tag{5}$$

where β is a positive constant.

Theorem 1. Under the control (5), all states of (4) will asymptotically converge to zero.

Proof. Select a Lyapunov function candidate: $V = s^2/2$. Differentiating V and substituting (4)-(5) yield,

$$\begin{aligned} \dot{V} &= s\dot{s} = s[c_1\dot{e}_1 + c_2\dot{e}_2 + c_3\dot{e}_3 + \dot{e}_4] \\ &= s[c_1x_2 + c_2f_1 + c_3 \frac{\partial f_1}{\partial f_3}x_4 + \frac{d}{dt}\left(\frac{\partial f_1}{\partial f_3}\right)x_4 + \frac{\partial f_1}{\partial f_3}\left(f_2 + \frac{1}{2k}U\right)] \\ &= -s \cdot \beta \text{sign}(s) = -\beta |s| \leq 0 \end{aligned} \tag{6}$$

For the controller (5), inequality (6) implies that the system can reach the surface, $s=0$, in finite time. β represents the amplitude of related to the sign-function, which has a relationship to the velocity of reaching the sliding surface. Since c_1, c_2, c_3 are selected to be positive constant numbers such that the polynomial $\lambda^3+c_3\lambda^2+c_2\lambda+c_1$ is Hurwitz, e_1, e_2 and e_3 will all converge to zero from any initial conditions. On the ideal sliding mode $s=0$, that is $e_4 = -c_1e_1 - c_2e_2 - c_3e_3$, e_4 will converge to zero too.

Then, we explain the vector $X=[x_1, x_2, x_3, x_4]^T$ will converge to 0 if $E \rightarrow 0$. From (4), we get that $e_1 = x_1, e_2 = x_2$ and $e_3 = f_1$ are stabilized. In practical

application, the current I and the air gap z are positive, so $x_3^*(=I/z)$ must be positive from Equation (2),

then $x_3(=x_3^* - \sqrt{mg/k})$ should be larger than in Equation (3). It follows that x_3 has to converge to zero from the stability of $e_3(=f_1 = -\frac{kx_3^2}{m} - 2\sqrt{\frac{kg}{m}}x_3)$. Similarly x_4 will converge to zero if e_4 is stabilized. Therefore, under the controller (5), the state variables of system (3) will all converge to the equilibrium point.

3. Adaptive Sliding Mode Controller Design

In order to eliminate the chattering typically found in conventional sliding mode control, we utilize the boundary layer technique [14,15,18]. If the control gain constant and the width of the boundary layer are fixed numbers, there is no guarantee for fast convergence. So we introduce an auto-tuning neuron to be the direct adaptive neural controller. The structure of an auto-tuning neuron can be mathematically expressed as [14,15,18]: $\sigma = E - \varphi$, where E represents the external input of neuron; φ denotes threshold of bias, and σ is the internal state of neuron.

The auto-tuning sliding mode control law for system (3) is

$$U = -\left[\frac{1}{2k} \frac{\partial f_1}{\partial f_3}\right]^{-1} \left\{c_1x_2 + c_2f_1 + c_3 \frac{\partial f_1}{\partial f_3}x_4 + \frac{d}{dt}\left[\frac{\partial f_1}{\partial f_3}\right]x_4 + \frac{\partial f_1}{\partial f_3}f_2\right\} + \phi(\sigma), \tag{7}$$

where $\phi(\sigma)$ is a modified hyperbolic tangent function,

$$\phi(\sigma) = \frac{a[1 - \exp(-b \cdot \sigma)]}{1 + \exp(-b \cdot \sigma)}, \tag{8}$$

where a is the saturated level; and b is the slope value. Obviously, the shape of the nonlinear saturated function is governed by the values of both a and b . Figure 2 gives the plot of (8), where two adjustable parameters a and b influence mainly the output range and the curve shape of the activation function. A larger b corresponds to a narrower boundary layer. Let $\theta = [a, b, \varphi]^T$ represent the vector of adjustable parameters.

In the following we will adjust θ to achieve the control objective. The auto-tuning law is designed as

$$\begin{aligned} \dot{a} &= -\eta e_1 \text{sign}\left(\frac{\partial x_1}{\partial U}\right) \left(\frac{1 - \exp(-b \cdot \sigma)}{1 + \exp(-b \cdot \sigma)}\right), \\ \dot{b} &= -\mu e_1 \text{sign}\left(\frac{\partial x_1}{\partial U}\right) a \sigma, \\ \dot{\varphi} &= -\dot{\sigma} = \gamma e_1 \text{sign}\left(\frac{\partial x_1}{\partial U}\right) a b, \end{aligned} \tag{9}$$

where η, μ and γ are positive constants used to ad-

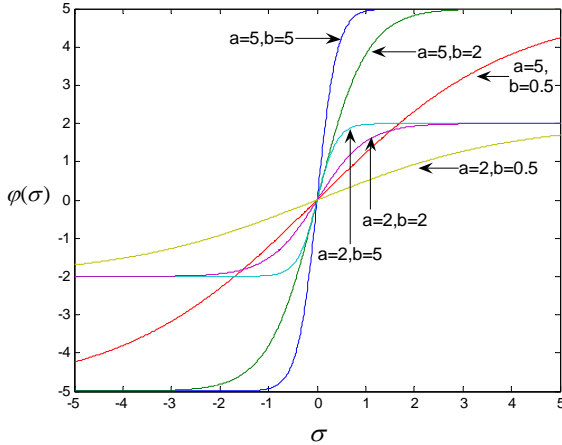


Figure 2. Modified activation function for different a and b .

just the convergence speed, and $\text{sign} \frac{\partial x_1}{\partial U}$ determines the direction of the search for θ . The accurate value of $\frac{\partial x_1}{\partial U}$ is not important since the maglev system output monotonically increases as the control input to the controlled plant increases, that is system (3) is said to be positive responded [18]. Then the system direction is written as 1. Fortunately, there are many industrial process control systems that possess the property of positive-responded or negative-responded.

Theorem 2. Under the control (7) and (8), all states of the system (3) with the adaptation law (9) will asymptotically converge to 0.

Proof. Consider the Lyapunov function candidate:

$$V = \frac{1}{2} e_1^2. \text{ Differentiating } V \text{ [14,15,18], we have}$$

$$\frac{dV}{dt} = \frac{\partial V}{\partial e_1} \frac{\partial e_1}{\partial x_1} \frac{\partial x_1}{\partial U} \left(\frac{\partial U}{\partial a} \frac{\partial a}{\partial t} + \frac{\partial U}{\partial b} \frac{\partial b}{\partial t} + \frac{\partial U}{\partial \sigma} \frac{\partial \sigma}{\partial \varphi} \frac{\partial \varphi}{\partial t} \right) \quad (10)$$

For convenience, denote the first term of the right hand side of (10) $V_1 = \frac{\partial V}{\partial e_1} \frac{\partial e_1}{\partial x_1} \frac{\partial x_1}{\partial U} \frac{\partial U}{\partial a} \frac{\partial a}{\partial t}$, the second term and the third $V_2 = \frac{\partial V}{\partial e_1} \frac{\partial e_1}{\partial x_1} \frac{\partial x_1}{\partial U} \frac{\partial U}{\partial b} \frac{\partial b}{\partial t}$,

$$V_3 = \frac{\partial V}{\partial e_1} \frac{\partial e_1}{\partial x_1} \frac{\partial x_1}{\partial U} \frac{\partial U}{\partial \sigma} \frac{\partial \sigma}{\partial \varphi} \frac{\partial \varphi}{\partial t}.$$

Substituting (7), (8) and (9) into (10) yield

$$V_1 = \frac{\partial V}{\partial e_1} \frac{\partial e_1}{\partial x_1} \frac{\partial x_1}{\partial U} \frac{\partial U}{\partial a} \frac{\partial a}{\partial t}$$

$$= e_1 \frac{\partial x_1}{\partial U} \frac{\partial}{\partial a} \left\{ - \left[\frac{1}{2k} \frac{\partial f_1}{\partial x_3} \right]^{-1} [c_1 x_2 + c_2 f_1 + c_3 \frac{\partial f_1}{\partial x_3} x_4 + \frac{d}{dt} \left(\frac{\partial f_1}{\partial x_3} \right) x_4 + \frac{\partial f_1}{\partial x_3} f_2] + \frac{a[1 - \exp(-b \cdot \sigma)]}{1 + \exp(-b \cdot \sigma)} \right\} \dot{a}$$

$$= -\eta e_1^2 \left| \frac{\partial x_1}{\partial U} \right| \left(\frac{1 - \exp(-b \cdot \sigma)}{1 + \exp(-b \cdot \sigma)} \right)^2 \leq 0$$

Similarly, V_2, V_3 become respectively:

$$V_2 = \frac{\partial V}{\partial e_1} \frac{\partial e_1}{\partial x_1} \frac{\partial x_1}{\partial U} \frac{\partial U}{\partial b} \frac{\partial b}{\partial t}$$

$$= -\mu e_1^2 \left| \frac{\partial x_1}{\partial U} \right| \frac{2 \exp(-b \cdot \sigma)}{(1 + \exp(-b \cdot \sigma))^2} a^2 \sigma^2 \leq 0,$$

$$V_3 = \frac{\partial V}{\partial e_1} \frac{\partial e_1}{\partial x_1} \frac{\partial x_1}{\partial U} \frac{\partial U}{\partial \sigma} \frac{\partial \sigma}{\partial \varphi} \frac{\partial \varphi}{\partial t}$$

$$= -\gamma e_1^2 \left| \frac{\partial x_1}{\partial U} \right| \frac{2 \exp(-b \cdot \sigma)}{(1 + \exp(-b \cdot \sigma))^2} a^2 b^2 \leq 0$$

where $e_1 \frac{\partial x_1}{\partial U}$ represents system output error contributed by the control input [18].

Since $\frac{dV}{dt} \leq 0$ while $V > 0$, according to the Lyapunov stability theory, V will decrease to zero, so $e_1 \rightarrow 0$, and $e_i (i = 2, 3, 4) = 0$. Therefore, similarly to the last paragraph in the proof of Theorem 1, the states of system (3) will all converge to zero.

4. Simulation and Results

In this section, we give the numerical simulation results of maglev system. The parameters and initial conditions used in the maglev system are given by $z_0 = 0.010m$, $m = 500kg$, $R = 4.4\Omega$, $k = 0.002$, $x(0) = (0.00458, 0, 1, 0)^T$. The parameters and initial conditions of the controller for simulation are $c_2 = 22.25$, $\eta, \mu, \gamma = 0.1$, $\beta = 0.1$, $\theta(0) = (-0.1, 0.2, 0)T$, and time interval is $t = 0.0001$,

As we know, the learning rate η, μ, γ play an important role in parameter learning process. For instance, a larger learning rate can accelerate the system response, but may also cause the system to have a larger overshoot. In the design of switching surface, $s = c_1 e_1 + c_2 e_2 + c_3 e_3 + e_4$, pole placement methodology [19] is often adopted to place the roots of the characteristic polynomial in desired region of the complex plane. That is, the control system denoted by the characteristic polynomial should have suitable damp, fast system response, short settling time and small overshoot. Therefore, c_1, c_2, c_3 are often chosen such that the three order polynomial has a pair of conjugate complex roots with negative real parts and a negative real root. When $c_1 = 21.75$, $c_2 = 22.25$, $c_3 = 8$, the roots of the characteristic polynomial are $-2.5 \pm li$ and -3 .

Our control object is to design the control input to regulate the air gap to the desired value. Figure 3(a) and (b) represent the performance of state x_1 and the control input U by using the traditional sliding mode con-

trol, and it can be seen that the chattering around $x_1 = 0$ have occurred. The control input is regulated with high-frequency, which is not expected in industrial field. Figure 4(a) and (b) show the results by using our proposed method. Here, we choose $c_1 = 12, c_2 = 14, c_3 = 6$. The state x_1 is asymptotically controlled to 0 and the control input U is modulated. In Figure 4(a), the regulation time of state x_1 is about 6 second and the overshoot is near to 0.6 mm. In Figure 4(b), the overshoot of control input is reduced to 2. These verify that better control performance of maglev system can be achieved by the proposed auto-tuning controller.

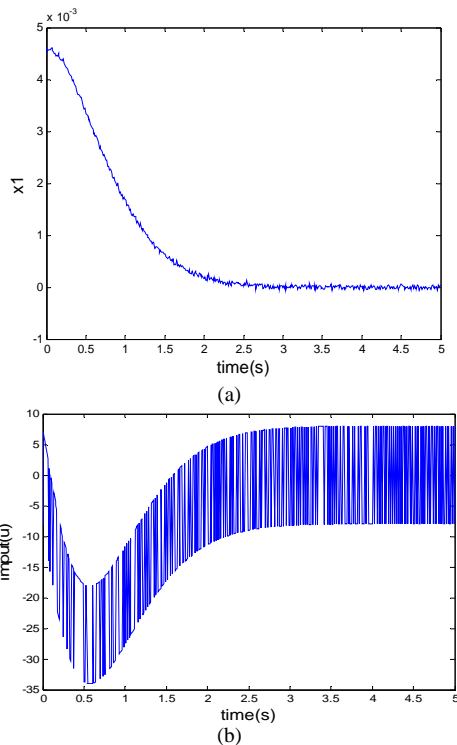


Figure3. (a-b) represent the control performance using the general sliding mode control.

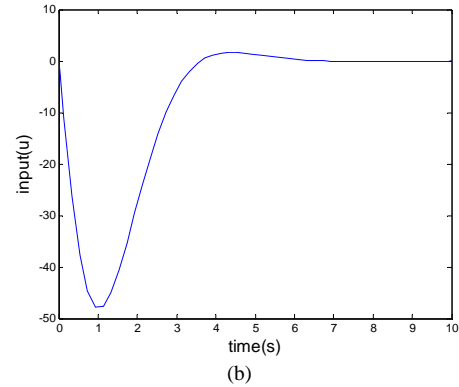
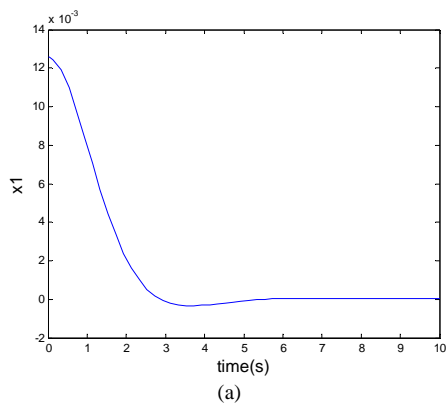


Figure 4. (a-b) show the results using the auto-tuning sliding mode control with control parameters $c_1=12, c_2=14, c_3=6$.

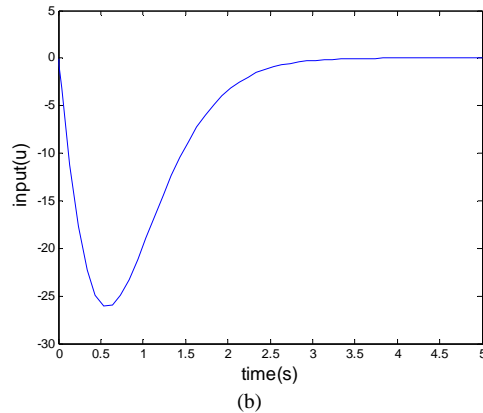
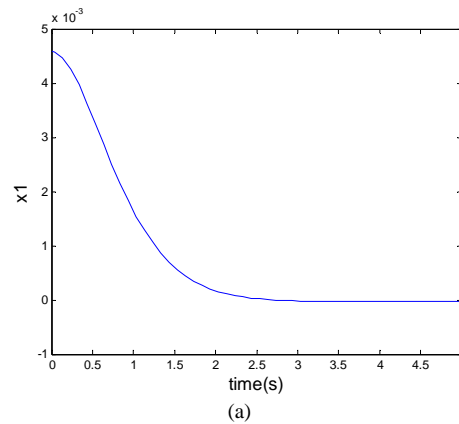


Figure 5. (a-b) show the results using the auto-tuning sliding mode control with control parameters $c_1=4, c_2=6, c_3=4$.

In Figure 4, the regulation time and overshoot is not satisfying, so here some new parameters $c_1 = 4, c_2 = 6, c_3 = 4$ by the proposed auto-tuning sliding mode control are chosen to accelerate system response and decrease the overshoot. In Figure 5(a), the convergence time of state x_1 slows to 3 second and the overshoot x_1 falls to 0. In Figure 5(b), the overshoot of control input is reduced to 0. It accords with the theoretical analysis. Based on the demand of practical application,

we can regulate these parameters to get a better performance.

5. Conclusions

In this paper, we discuss the problem of vibration control of maglev problem via a sliding mode control approach. In order to eliminate the high control activity and chattering caused by the general sliding mode control, we present an auto-tuning law based on the Lyapunov stability theory to guarantee the convergence of the system states. Simulation results verify the proposed auto-tuning controller is better than the traditional sliding mode controller.

It should be pointed out that only three control parameters are chosen to achieve good performance for maglev system in this paper, but other factors also can be applied to sliding mode control in practice. Next plan is to combine with more state variables with elastic guideway conditions. The expected results should improve the suspension performance of flexible guideway with proposed control algorithms.

6. References

- [1] Y. Yoshihide, F. Masaaki, T. Masao, *et al*, "The first HSST maglev commercial train in Japan," *MAGLEV 2004 Proceedings*, pp. 76–85, 2004.
- [2] R. Goodall, "Dynamic and control requirements for EMS maglev suspension," *MAGLEV 2004 Proceedings*, pp. 926–934, 2004.
- [3] H. Wang, J. Li, K. Zhang, "Non-resonant response, bifurcation and oscillation suppression of a non-autonomous system with delayed position feedback control," *Nonlinear Dynamic*, Vol. 51, pp. 447–464, 2008.
- [4] L. Zhang, L. Huang, Z. Zhang, "Stability and Hopf bifurcation of the maglev system with delayed position and speed feedback control," *Nonlinear Dynamic*, Vol. 57, pp. 197–207, 2009.
- [5] C. Feng, W. U. Zhu, "Stochastic optimal control of strongly nonlinear systems under wide-band random excitation with actuator saturation," *Acta Mechanica Sinica*, Vol. 21, No. 2, pp. 116–126, 2008.
- [6] N. Taher, "A new fuzzy adaptive hybrid particle swarm optimization algorithm for non-linear, non-smooth and non-convex economic dispatch problem," *Applied Energy*, doi:10.1016/j.apenergy.2009.05.016, 2009.
- [7] H. Tomohisa, M. Wassim, Y. Konstantin, "Neural network hybrid adaptive control for nonlinear uncertain impulsive dynamical systems," *Nonlinear Analysis: Hybrid Systems*, Vol. 2, pp. 862–874, 2008.
- [8] V. Suplina, U. Shaked, "Robust H1 output-feedback control of systems with time-delay," *Systems and Control Letters*, Vol. 57, No. 3, pp. 193–199, 2008.
- [9] B. Giorgio, F. Leonid, P. Alessandro, *et al*, "Modern sliding mode control theory," Berlin, Spinker, 2008.
- [10] J. J. Slotine, W. Li, "Applied nonlinear control," Englewood Cliffs (NJ), Prentice-Hall, 1991.
- [11] Y. J. Huang, T. C. Kuo, "Robust position control of DC servomechanism with output measurement noise," *Electrical Engineering*, Vol. 88, pp. 223–338, 2006.
- [12] K. Furuta, "VSS type self-tuning control," *IEEE Transactions on Industrial Electronics*, 40, pp. 37–44, 1993.
- [13] P. M. Lee, J. H. Oh, "Improvements on VSS type self-tuning control for a tracking controller," *IEEE Transactions on Industrial Electronics*, Vol. 45, pp. 319–325, 1998.
- [14] C. T. Chen, W. D. Chang, "A feedforward neural network with function shape autotuning," *Neural Networks*, Vol. 9, No. 4, pp. 627–641, 1996.
- [15] W. D. Chang, R. C. Hwang, J. G. Hsieh, "Application of an auto-tuning neuron to sliding mode control," *IEEE Transactions on Systems, Man, and Cybernetics-Part C*, Vol. 32, pp. 517–529, 2002.
- [16] T. C. Kuo, J. H. Ying, S. H. Chang, "Sliding mode control with self-tuning law for uncertain nonlinear systems," *ISA Transactions*, Vol. 47, pp. 171–178, 2008.
- [17] X. Rong, Ä. O. ÄUmit, "Sliding mode control of a class of underactuated systems," *Automatica*, Vol. 44, pp. 233–241, 2008.
- [18] X. Cui, K. G. Shin, "Direct control and coordination using neural networks," *IEEE Transactions on Systems, Man, and Cybernetics*, Vol. 23, No. 3, pp. 686–697, 1993.
- [19] C. D. Richard, H. B. Rober, "Modern control systems," Addison Wesley Longman, 1993.

The Research on Adaptive Control Modeling of a Liquid Fertilizer Spreader

Zidong Yang

School of Agriculture Engineering and Light Industry, Shandong University of Technology, Shandong, China

E-mail: Yzd@sdut.edu.cn

Received September 28, 2009; revised October 22, 2009; accepted October 28, 2009

Abstract

This paper describes a general modeling and control approach for steering wheel variable rate liquid fertilizer applicator. An adaptive numerical modeling approach for describing the system input-output dynamics is proposed, and an optimal control that accounts for the control hardware limits is developed. Field tests have demonstrated the effectiveness of the theoretical development.

Keywords: Adaptive Control, Variable Rate Fertilizer, Precision Agriculture, Optimal Control, Manure Spreader

1. Introduction

Based on a set of high-new technologies, such as the modern information technology, the organism technology and the engineering technology, etc., the precision agriculture has become the important way of modern agricultural production. Compared with foreign developed countries, the intensive level is quite low in China. However, according to the characteristics of the agricultural development in China, the technological system of water-saving and variable rate fertilizer should be developed in the near future. The precision equipped agriculture can be implemented firstly in the region where the equipped agriculture has been developed fast. For example, the big farms, which have large scales and high mechanization level, may carry on the practice of the precision agriculture.

Fertilizer-saving precision agriculture can not only decrease costs, but also increase yields. Furthermore, accurately applying chemicals and fertilizers only where needed can reduce the potential for ground and surface water pollution. Manure produced by livestock contains valuable nutrients for crops. Additional fertilizers are often applied to increase the crop production. Excessive applied manure and fertilizer contributes to ground and surface water pollution and also increases the cost of crop production. So there is a need to develop an automated spreader in order to achieve consistent and precise application of crop nutrients.

Straub *et al.* (1998) described a computer controlled manure spreader developed by John Deere Corporation in collaboration with the University of Wisconsin-Madison, and carried out field tests indicating that the

control system worked well with lighter and dryer manure. One of the problems they faced is how to measure the manure discharge. In their control system, the weight of the spreader is measured over time and a finite difference method is used to compute the discharge rate. High-performance controllers, including a supervisory control and a control with a Kalman filter and a Smith predictor for time delay, have been developed by [1]. Magnetic inductive flow meters are used to measure the manure's flow rate. Landry *et al.* [2,3] recently studied physical and rheological properties of manure and investigated the effectiveness of conveying systems for manure spreaders.

The present study is on a system on-line identification algorithm. A numerical regression model is designed to describe the input-output dynamics of the spreader. The parameters of the numerical model are updated in real time to account for the time varying and nonlinear properties of the spreader dynamics.

The remainder of the paper is organized as follows: in the section below, we describe the objectives of the research and a description of the hardware and software system. Then we present a discussion of numerical modelling of the input-output dynamics of the spreader and an experimental validation of the model. The adaptive optimal control for regulating the discharge rate of the spreader is subsequently developed.

2. Research Objectives and System Description

Because China has a large number of small and medium sized tractors, in order to increase output, the mulch

sowing and straw returning has been widely popularized. But this has caused some difficulties for variable-rate fertilization and deep fertilization of the liquid fertilizer. The general variables spraying method can't adapt to this situation. With regards to this, we have designed a steering wheel variable rate manure spreader and the adaptive control system, which is more suitable for medium-small size tractors, variable-rate fertilization and deep fertilization to the liquid fertilizer. A picture of the machine is shown in Figure 1. The auger speed and the gate opening size can be controlled. The objective of the control algorithm is to regulate these two quantities for a pre-determined spreading application density per unit area. As an example, the control task set for the present study is to attain a specified constant discharge mass per unit area from the spreader taking into account varying speed of the tractor and the material variability of the semi-solid animal wastes. This manure spreader used variable rate technologies (VRT) describes machines that can automatically change their application rates in response to their position.

The core of the VRT system is the flow rate controller. Essentially, the flow control system receives the set point flow rate from the application system (likely a GPS/GIS system) on-board the tractor and then manipulates a number of actuators in an attempt to adjust the actual flow-rate to match the set-point.

To provide a specific illustration, consider the diagram of a relatively simple liquid sprayer VRA system as depicted in Figure 2. The following discussion is provided as one scenario for each component, but there may be alternative sensors and methods of control. A radar based ground speed sensor would be used to provide true ground speed to the computer/controller since application rate is a function of speed. This system depicts the use of a direct injection sprayer, which is the direction in

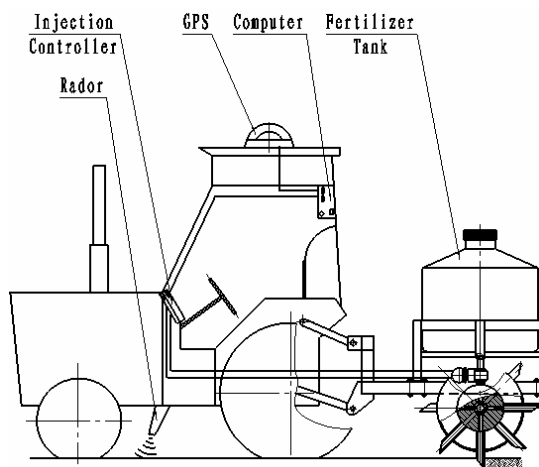


Figure 1. Schematic representation of the components of a VRT manure spreader.

which sprayer technology is proceeding. With this type of sprayer, the operator does not mix the chemical(s) in the main tank, rather, the chemical(s) remains in a container, where it may be pumped as needed into an injector where the chemical(s) is automatically mixed with water on-the-fly. There are many advantages to this system as compared with tank-mixing, such as safety, managing mixed chemicals, and automation. The injector pump may be designed to provide precise control of the injection rate of the chemical concentrate to the injector. The water tank may have a level sensor which will allow the computer/controller to determine the amount of water remaining in the tank in gallons. The total flow rate of the fluid going to the boom(s) will be controlled by the flow control valve, which in turn is controlled by the computer/controller. The actual total fluid flow rate will be monitored by the fluid flow rate sensor, and this information will be used by the computer/controller for fine adjustments in the flow control valve. The fluid flow rate and the vehicle position will be continuously recorded in the computer as the vehicle sprays to provide a historical record for the GIS about where and how much chemical was dispensed. The boom valve will be used to turn the boom on or off to provide fast accurate control of the application area.

The controllers are very similar to those used on many sprayers, spreaders and other agricultural machines. On conventional machines, the operator controls the application rate by selecting the desired rate from the console panel in the cab. It is assumed that the spreading width of the material is a constant. Note that the auger speed is adjusted by varying the swash plate angle of the

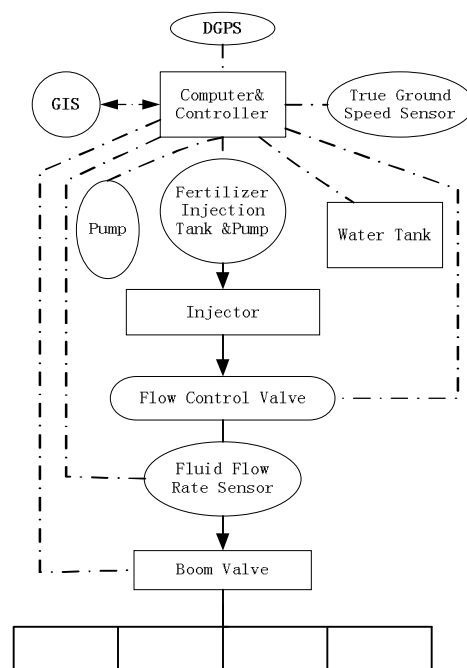


Figure 2. The sketch map of liquid fertilizer sprayer.

hydraulic pump. In order to develop control algorithms to achieve the above objective, we must first develop a dynamic model for the spreader. Specifically, we need a relationship between the input, i.e. the auger speed and the gate opening size, and the output, i.e. the material discharge rate. Recall that the material is a highly inhomogeneous mix of liquids and solids with unknown percentage of each phase. The weight and viscosity of the material affect the dynamics of the hydraulic system that drives the auger. As the spreading proceeds, the amount of material remaining in the tank changed. All these factors attribute to a nonlinear and time-varying dynamics of the spreader. As discussed in Section 1, analytical modeling of such a system is a difficult task. In this study, we propose to develop an on-line numerical model of the input-output relationship, known as the system transfer function. The controller of on-line model has an Atmel processor 89S51 with 33MHz frame rate. It communicates with a laptop computer via RS232 at 9600 baud. This controller can interface with and control a wide range of equipment including variable rate applicators for precision agriculture. The on-line system model fits the experimental data to a pre-determined numerical model with undetermined coefficients. A very common numerical model can describe a large.

3. On-Line System Modeling

Class of dynamic systems is the autoregressive model with exogenous inputs (ARX) (Billings, 1986; Diaz and Desrochers, 1988; Ljung, 1987). It is given in a general form as

$$\begin{aligned} y_n + a_1 y_{(n-1)} + \dots + a_{n_a} y_{(n-n_a)} \\ = b_1 u_{(n-n_k)} + \dots + b_{n_b} u_{(n-n_k-n_b+1)} \end{aligned} \quad (1)$$

The current output y_n is assumed to be a function of a finite history of output values $y_{(n-1)}$ to $y_{(n-n_a)}$ and the delayed input $u_{(n-n_k)}$ to $u_{(n-n_k-n_b+1)}$. The coefficients $a_i (i=1, \dots, n_a)$ and $b_j (j=1, \dots, n_b)$ are undetermined. The on-line modeling algorithm determines the coefficients and approximates the numerical model to the measured system dynamics in some optimal manner.

Strictly speaking, the ARX model is valid for linear dynamic systems. The present spreader system is time varying and nonlinear. A properly identified ARX model will accurately represent the dynamics of the system over a short time interval and will not be valid for the entire history of the spreading task from a full tank to empty. Therefore the ARX model must be updated frequently during spreading. Efficient real-time adaptive algorithms will be needed for this task.

3.1. Adaptive Algorithm

In signal processing, the ARX model is also known as an

infinite impulse response (IIR) filter (Haykin, 1991). A popular steepest gradient descent method known as the least mean square (LMS) algorithm (Widrow and Stearns, 1985) can be used to adjust the coefficients of the ARX model and minimize the error between the prediction of the numerical model and the real measurement. The estimation error is $e_k = d_k - y_k$, where d_k is the measured output and y_k is the predicted output. A performance index can be defined as $J(k) = e_k^2$. We write the ARX model in a vector notation as

$$y_k = \mathbf{w}_k^T \mathbf{u}_k \quad (2)$$

where \mathbf{w}_k^T is a vector consisting of the undetermined coefficients at the k th time step and \mathbf{u}_k is a vector consisting of both the past history of y_k and the control inputs. The LMS algorithm for updating the undetermined coefficients in order to minimize $J(k)$ is given by

$$\mathbf{w}_{(k+1)} = \mathbf{w}_k + \beta e_k \mathbf{u}_k \quad (3)$$

where β is an adaptation gain parameter.

3.2. Experimental Validation of the LMS Algorithm

We have selected a simple ARX model for the spreader given by

$$y_k = a_1 y_{(k-1)} + a_2 u_{(k-1)}^s + a_3 u_{(k-1)}^g \quad (4)$$

where $u_{(k-1)}^s$ denotes the swash plate angle that regulates the auger speed and $u_{(k-1)}^g$ is the rear gate opening. We have carried out experiments to compare this simple model with more complicated ones, and found that this model describes the system with a good balance of accuracy and efficiency, and is sufficient for our work. A digital second order IIR low pass filter of bandwidth 2Hz programmed in the C language is used to block noise in the weight signal. The weight signal is sampled at a rate of 100 Hz in real time. During spreading, the gate positions are fixed for a period of time during which the swash plate is swept from being completely closed to being fully open to adjust the auger speed. The purpose of doing so is to create a set of data from one test run that excites as much of the system dynamics as possible. The model prediction is seen to be quite accurate. The parameter a_1 is nearly equal to one. This is physically reasonable since in the absence of the control, i.e. when the auger speed is zero and the gate is closed, the material remaining in the tank is unchanged. The parameters a_2 and a_3 are negative. It is again physically reasonable that a_2 and a_3 are negative. When the control inputs are greater than zero, the material remaining in the tank y_k decreases. The ranges of these coefficients are as follows:

$\max(a_1)=1.0047$, $\min(a_1)=0.9881$, average $a_1=1.0011$;
 $\max(a_2)=-0.0083$, $\min(a_2)=-0.0111$, average $a_2=-0.0094$;
 $\max(a_3)=-0.0045$, $\min(a_3)=-0.0080$, average $a_3=-0.0063$.

4. Control Algorithm

The control algorithm design depends on the system model. This section focuses on a discussion of the control algorithm design. The integration of the control loop and the parameter updating loop is natural and is coded in the software.

4.1. Range Limited Optimal Control

Lewis and Syrmos [4] have shown that after going through the steps of optimal control solutions and taking $i=k$ and $N=k+1$, we obtain the unconstrained optimal control solution as

$$u_k^* = -(R + c_k c_k^T sN)^{-1} c_k sN (a_1 e_k + G_k) \quad (5)$$

We shall continue the study with the one step optimal control. Recall that the range of u_k^s and u_k^g is finite. The unconstrained optimal solution (5) is valid when the bound is not exceeded. To account for the bounds on the controls, we need to use the Pontryagin's minimum principle. This leads to the following inequality for determining the control u_k^* :

$$\frac{1}{2} u_k^{*T} R u_k^* + I_{k+1}^T c_k^T u_k^* \leq \frac{1}{2} u_k^T R u_k + I_{k+1}^T c_k^T u_k \quad (6)$$

The inequality holds for all admissible values of u_k . The optimal control can be found from the inequality by considering an auxiliary problem of minimization of the following quadratic form:

$$w = \frac{1}{2} (u_k + R^{-1} c_k I_{k+1})^T (u_k + R^{-1} c_k I_{k+1}) \quad (7)$$

It can be shown that the u_k that minimizes w also minimizes the left hand side of the inequality (5). Let the lower and upper bounds of the control be denoted by $u_{k_{\min}}^{s,g}$ and $u_{k_{\max}}^{s,g}$. Let $u_k^{s,g}$ denote the swash plate and gate opening control elements of the vector in Equation 5, i.e.:

$$u_k^{s,g} = [-(R + c_k c_k^T sN)^{-1} c_k sN (a_1 e_k + G_k)]^{s,g} \quad (8)$$

After several algebraic steps, we obtain the range constrained optimal control as

$$u_k^{*s,g} = \begin{cases} u_{k_{\min}}^{s,g}, U_k^{s,g} \leq u_{k_{\min}}^{s,g} \\ U_k^{s,g}, u_k^{s,g} < U_k^{s,g} < u_{k_{\max}}^{s,g} \\ u_{k_{\max}}^{s,g}, U_k^{s,g} \geq u_{k_{\max}}^{s,g} \end{cases} \quad (9)$$

The middle branch of the solution is the same as that in Equation 5. In other words, when the system operates within the physical limits of the controls, the solution given by Equation 5 is optimal. Note that when the num-

ber of inputs is greater than the number of outputs, the matrix R cannot be zero, and has to be positive definite.

4.2. Rate Limited Optimal Control

The range limited optimal control problem implies that the controls can be instantly switched from one level to another. This is of course not realistic since a physical device always takes a finite time to change and has inherent delays. When the controller requires the system to change faster than the physical rate limit, rate saturation occurs. To account for the rate limits, we once again invoke the Pontryagin's minimum principle and consider the increment Δu_{k-1} such that $u_k = u_{k-1} + \Delta u_{k-1}$ as the control variable. Applying the Pontryagin's minimum principle in terms of the control increment, we have another inequality

$$\begin{aligned} & \frac{1}{2} (u_{k-1}^* + \Delta u_{k-1}^*)^T R (u_{k-1}^* + \Delta u_{k-1}^*) + I_{k+1}^T c_k^T (u_{k-1}^* + \Delta u_{k-1}^*) \\ & \leq \frac{1}{2} (u_{k-1} + \Delta u_{k-1})^T R (u_{k-1} + \Delta u_{k-1}) + I_{k+1}^T c_k^T (u_{k-1} + \Delta u_{k-1}) \end{aligned} \quad (10)$$

The optimal control increment can be found from the inequality by considering an auxiliary problem of minimization of the following quadratic form:

$$w = \frac{1}{2} (u_{k-1} + \Delta u_{k-1} R^{-1} c_k I_{k+1})^T (u_{k-1} + \Delta u_{k-1} + R^{-1} c_k I_{k+1}) \quad (11)$$

Define an increment by using Equation 8 as

$$\Delta U_k^{s,g} = U_k^{s,g} - U_{k-1}^{s,g} \quad (12)$$

By minimizing w with respect to Δu_{k-1} , we obtain the optimal control increment as

$$\Delta u_{k-1}^{*s,g} = \begin{cases} \Delta U_k^{s,g} & |\Delta U_{i,k}| \leq \Delta u_{k_{\max}}^{s,g} \\ \text{sgn}(\Delta U_k^{s,g}) \Delta u_{k_{\max}}^{s,g} & |\Delta U_{i,k}| > \Delta u_{k_{\max}}^{s,g} \end{cases} \quad (13)$$

where $\Delta u_{k_{\max}}^{s,g}$ denotes the physically allowable maximum rate of change of the swash plate and rear gate controls over one sample interval. The top branch of the solution matches the range limited optimal control and the lower branch is the rate saturated control. By combining Equations 5 and 13, we obtain the optimal control under both range and rate saturation limits. More discussions of such optimal control problems can be found in Kobs and Sun (1997).

5. Discussions and Conclusions

In order to attain the goal of saving fertilizer, cutting down production cost and protecting environment, the liquid fertilizer applicator was designed and tested in field trial based on its advantages of non-dust, non-smog and reducing environment pollution during the process of production, usage and transportation. The optimized working

parameters by means of field trial were as follows: fertilization depth of 60-100 mm, operation velocity of 1.3m/s and pump working pressure of 0.36 MPa. Let D_A denotes the required mass per unit area (kg/m^2). The spreading width is 1.5 m. A relationship between the discharge rate D_t per unit time (kg/s), the speed of the tractor v (m/s) and D_A can be found as $D_t = 4.167vD_A (\text{kg}/\text{s})$. Since the discharge rate is constant when the tractor speed is constant, the material remaining in the tank is a linearly decreasing function of time. The actual measurement is in good agreement with the reference input. Note that there is significant noise in the measurement due to vehicle dynamics and electronic disturbances. The low pass digital filter designed for the weight sensor is quite effective in reducing measurement noise.

We have presented a general modeling and control approach for precision agricultural applications by using a SYF-2 manure spreader as an example. The numerical input-output modeling approach can handle a wide range of variations in manure materials and the complicated nonlinear dynamics of the machine. The adaptive self-tuning optimal control algorithm can cope with various hardware limits. The theoretical development has been validated by extensive experimental results. The present approach provides a promising methodology for automat-

ing machines for precision agricultural applications.

6. Acknowledgments

This paper supported by National Key Technology R&D Program during the 11th Five-Year Plan Period of China (2006BAD11A17) and the visiting scholar project of excellent young teachers of higher learning in Shandong Province.

7. References

- [1] A. Munack, E. Buning, H. Speckmann, "A high-performance control system for spreading liquid manure," *Control Engineering Practice*, Vol. 9, pp. 387–391, 2001.
- [2] H. Landry, C. Lague, and M. Roberge, "Physical and rheological properties of manure products," *Applied Engineering in Agriculture*, Vol. 20, No. 3, pp. 277–288, 2004.
- [3] H. Landry, E. Piron, J. M. Agnew, C. Lague, M. Roberge, "Performances of conveying systems for manure spreaders and effects of Hopper geometry on output flow," *Applied Engineering in Agriculture*, Vol. 21, No. 2, pp. 159–166, 2005.
- [4] F. L. Lewis, V. L. Symos, "Optimal control," John Wiley and Sons, Inc., New York, 1995.

A Set of Globally Stable N-PID Regulators for Robotic Manipulators

Baishun Liu, Fancai Lin, Bingli Tian

Department of Battle & Command, Academy of Naval Submarine, Qingdao, China
 E-mail: baishunliu@163.com, lfcai_777@yahoo.com.cn, woshixiaobenmiao@126.com
 Received August 28, 2009; revised September 28, 2009; accepted October 4, 2009

Abstract

This paper deals with the position control of robot manipulators with uncertain and varying-time payload. Proposed is a set of novel N-PID regulators consisting of a linear combination of the proportional control mode, derivative control mode, nonlinear control mode shaped by a nonlinear function of position errors, linear integral control mode driven by differential feedback, and nonlinear integral control mode driven by a nonlinear function of position errors. By using Lyapunov's direct method and LaSalle's invariance principle, the simple explicit conditions on the regulator gains to ensure global asymptotic stability are provided. The theoretical analysis and simulation results show that: an attractive feature of our scheme is that N-PID regulators with asymptotic stable integral actions have the faster convergence, better flexibility and stronger robustness with respect to uncertain and varying-time payload, and then the optimum response can be achieved by a set of control parameters in the whole control domain, even under the case that the payload is changed abruptly.

Keywords: Manipulators, Robot Control, PID Control, N-PID Control, Global Stability

1. Introduction

It is well known that PID controllers can effectively deal with nonlinearity and uncertainties of dynamics, and asymptotic stability is achieved accordingly [1–3]. Hence, most robots employed in industrial operations are controlled through PID controllers that introduce integral action by integrating the error. It is well known that integral-action controllers with this class of integrator often suffer a serious loss of performance due to integrator windup, which occurs when the actuators in the control loop saturate. Actuator saturation not only deteriorates the control performance, causing large overshoot and long settling time, but also can lead to instability, since the feedback loop is broken for such saturation. To avoid this drawback, various PID-like controllers have been proposed to improve the transient performance. For example, PID controllers consisting of a saturated-P, and differential feedback plus a PI controller driven by a bounded nonlinear function of position errors [4], a linear PD feedback plus an integral action of a nonlinear function of position errors [5], a linear derivative feedback plus a PI term driven by a nonlinear function of position errors [1], a linear PD feedback plus double integral action driven by the positions error and the filtered

position [6], a linear PD feedback plus an integral action driven by PD controller [7], and a linear PD feedback plus an integral action driven by NP-D controller [8], are presented recently.

In this paper, we propose a set of new global position controllers for robots which do not include their dynamics in the control laws. Motivated by the idea that is introducing the nonlinear action of the position errors into PD-NI controller [5] and modifying the nonlinear integral action via injection of the required damping so that the transient performance of the closed-loop system may be improved, we develop a set of new N-PID-like regulators consisting of a linear combination of the proportional control mode, derivative control mode, nonlinear control mode shaped by a nonlinear function of position errors, linear integral control mode driven by differential feedback, and nonlinear integral control mode driven by a nonlinear function of position errors. The simple explicit conditions on the regulator gains to ensure global asymptotic stability are provided.

Throughout this paper, we use the notation $\lambda_m(A)$ and $\lambda_M(A)$ to indicate the smallest and largest eigenvalues, respectively, of a symmetric positive definite bounded matrix $A(x)$, for any $x \in R^n$. The norm of vector x is defined as $\|x\| = \sqrt{x^T x}$, and that of matrix A

is defined as the corresponding induced norm $\|A\| = \sqrt{\lambda_M(A^T A)}$.

The remainder of the paper is organized as follows. Section 2 summarizes the robot model and its main properties. Our main results are presented in Sections 3 and 4, where we briefly review some known PID-like control laws and present a set of new N-PID-like control laws, and then provide the conditions on the controller gains to ensure global asymptotic stability, respectively. Simulation examples are given in Section 5. Conclusions are presented in Section 6.

2. Problem Formulation

The dynamic system of an n -link rigid robot manipulator system [1] can be written as:

$$M(q)\ddot{q} + C(q, \dot{q})\dot{q} + D\dot{q} + g(q) = u \quad (1)$$

where q is the $n \times 1$ vector of joint positions, u is the $n \times 1$ vector of applied joint torques, $M(q)$ is the $n \times n$ symmetric positive definite inertial matrix, $C(q, \dot{q})\dot{q}$ is the $n \times 1$ vector of the Coriolis and centrifugal torques, D is the $n \times n$ positive definite diagonal friction matrix, and $g(q)$ is the $n \times 1$ vector of gravitational torques obtained as the gradient of the robot potential energy $U(q)$ due to gravity.

A list of properties [1] of the robot dynamic model (1) is recalled as follows:

$$0 < \lambda_m(M) \leq \|M(q)\| \leq \lambda_M(M) \quad (2)$$

$$\zeta^T (\dot{M}(q) - 2C(q, \dot{q})) \zeta = 0 \quad \forall \zeta \in R^n \quad (3)$$

$$0 < C_m \|\dot{q}\|^2 \leq \|C(q, \dot{q})\dot{q}\| \leq C_M \|\dot{q}\|^2 \quad \forall q, \dot{q} \in R^n \quad (4)$$

where C_m and C_M are all positive constants.

For the purpose of this paper, it is convenient to introduce the following definition and properties [5].

Definition 1: $F(\alpha, \beta, x)$ with $1 \geq \alpha > 0$, $\beta > 0$, and $x \in R^n$ denotes the set of all continuous differential increasing functions,

$f(x) = [f(x_1), \dots, f(x_n)]^T$ such that

$$\begin{aligned} |x| \geq |f(x)| &\geq \alpha |x| & \forall x \in R: |x| < \beta \\ \beta \geq |f(x)| &\geq \alpha \beta & \forall x \in R: |x| \geq \beta \\ 1 &\geq (d/dx)f(x) \geq 0 \end{aligned} \quad (5)$$

where $|\bullet|$ stands for the absolute value.

Figure 1 depicts the region allowed for functions belonging to set $F(\alpha, \beta, x)$. For instance, the tangent hyperbolic function belongs to set $F(\tanh(1), 1, x)$ and the Arimoto sine function, whose entries are given as follows:

$$f(x) = \begin{cases} 1 & \text{if } x \geq \pi/2 \\ \sin(x) & \text{if } |x| < \pi/2 \\ -1 & \text{if } x \leq -\pi/2 \end{cases} \quad (6)$$

which belongs to set $F(\sin(1), 1, x)$.

The important properties of function $f(x)$ belonging to set $F(\alpha, \beta, x)$ are now established.

The function $x^T f(x)$ satisfies for all $x \in R^n$,

$$x^T f(x) \geq 0 \quad (7)$$

The Euclidean norm of $f(x)$ satisfies for all $x \in R^n$,

$$\|f(x)\|^2 \leq \|x\|^2 \quad (8)$$

$$\|f(x)\| \leq \sqrt{n}\beta \quad (9)$$

Throughout this paper, we use the notation $\Delta q = q - q_d$, to indicate the position errors, q_d is the desired joint position, which is assumed to be constant; K_p , K_D , K_s , K_{pf} , K_I , K_{IP} and K_{ID} are all positive definite diagonal $n \times n$ matrices.

3. N-PID-Like Control Laws

3.1. PID-Like Control Law Review

To put our contribution in perspective, we will briefly review some known PID-like control laws, as follows:

1) Semiglobally stable PID control law [1],

$$u = -K_p \Delta q - K_D \dot{q} - K_I \int_0^t \Delta q(\tau) d\tau.$$

2) Globally stable PD-NI control law [1],

$$u = -K_p \Delta q - K_D \dot{q} - K_I \int_0^t \tanh(\Delta q(\tau)) d\tau.$$

where $\tanh(\bullet)$ is the hyperbolic tangent vector function.

3) Globally stable PD-NPI control law [1],

$$u = -K_p \Delta q - K_D \dot{q} - K_s s(\Delta q) - K_I \int_0^t s(\Delta q(\tau)) d\tau.$$

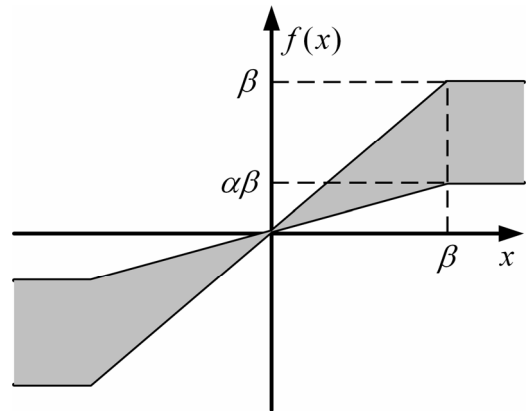


Figure 1. $F(\alpha, \beta, x)$ functions.

where $s(\bullet)$ is the differential function of a class of approximate potential energy function.

4) Semiglobally stable PI²D control law [6],

$$u = -K_p \Delta q - K_D \dot{q} - K_I \int_0^t [\Delta q(\tau) + \Delta \dot{q}(\tau)] d\tau .$$

5) Semiglobally stable PD-I^{PD} control law [7],

$$u = -K_p \Delta q - K_D \dot{q} - \int_0^t [K_{IP} \Delta q(\tau) + K_{ID} \Delta \dot{q}(\tau)] d\tau .$$

6) Globally stable PD-I^{NP-D} control law [8],

$$u = -K_p \Delta q - K_D \dot{q} - \int_0^t [K_{IP} \tanh(\Delta q(\tau)) + K_{ID} \Delta \dot{q}(\tau)] d\tau .$$

7) Globally stable SP-D-NPI control law [4],

$$u = -K_p \text{sat}(\Delta q) - K_D \dot{q} - K_{pf} f_b(\Delta q) - K_I \int_0^t f_b(\Delta q(\tau)) d\tau$$

where $\text{sat}(\bullet)$ is the normal saturated function and $f_b(\bullet)$ is a bounded nonlinear function.

8) Globally stable PD-NI control law [5],

$$u = -K_p \Delta q - K_D \dot{q} - K_I \int_0^t f(\Delta q(\tau)) d\tau \quad (10)$$

where $f(\bullet)$ is a continuous differential increasing bounded functions shown in Figure 1.

Most of the present industrial robots are controlled through PID-like controllers above. Although these controllers have been shown in practice to be effective for position control of robot manipulators, unfortunately most of them often suffer a serious loss of performance, that is, causes large overshoot and long settling time due to unlimited integral action.

Based on the above fact, we get intuitively an idea that the transient performance of the closed-loop system may be improved if the nonlinear action of position errors is introduced into the control law (10) and the damping is injected into its integrator. Following this idea, a set of novel N-PID-like regulators is developed in the next subsection.

3.2. Our N-PID Control Laws

The new nonlinear PID control laws are proposed as follows,

$$u = -K_p \Delta q - K_D \dot{q} - K_{pf} f(\Delta q) - \int_0^t [K_{IP} f(\Delta q(\tau)) + K_{ID} \Delta \dot{q}(\tau)] d\tau \quad (11)$$

It is worthy to note that the control law above is consisting of a linear combination of the proportional control mode, derivative control mode, nonlinear control mode, linear integral control mode and nonlinear integral control mode. Hence, based on the five control modes above, five differential N-PID-like control laws with the same stability

as the control law (11) can be derived, as follows:

$$u = -K_p \Delta q - K_D \dot{q} - \int_0^t [K_{IP} f(\Delta q(\tau)) + K_{ID} \Delta \dot{q}(\tau)] d\tau \quad (12)$$

$$u = -K_D \dot{q} - K_{pf} f(\Delta q) - \int_0^t [K_{IP} f(\Delta q(\tau)) + K_{ID} \Delta \dot{q}(\tau)] d\tau \quad (13)$$

$$u = -K_D \dot{q} - \int_0^t [K_{IP} f(\Delta q(\tau)) + K_{ID} \Delta \dot{q}(\tau)] d\tau \quad (14)$$

$$u = -K_p \Delta q - K_D \dot{q} - K_{IP} \int_0^t f(\Delta q(\tau)) d\tau \quad (15)$$

$$u = -K_p \Delta q - K_D \dot{q} - K_{pf}(\Delta q) - K_{IP} \int_0^t f(\Delta q(\tau)) d\tau \quad (16)$$

Discussion 1: It is obvious that the control law (11) can be simplified to other PID-like control laws such as P-NI control, NPI control, PD-I^{NP-D} control [8], and so on. Moreover, the control law (15) is the same as the one (10) reported by [5]. This shows that the control law (11) is a natural extension of them and implies that its application is not limited in the robots, too.

Discussion 2: Notice that the integral actions in control laws (10) and (11) can be rewritten as $\dot{\sigma} = -K_I f(\Delta q)$ and $\dot{\sigma} = -K_{IP} f(\Delta q) - K_{ID} \Delta \dot{q}$, respectively. From this, it is easy to see that the latter has the same stability as the one presented by [7,8], that is, they are all asymptotically stable but the former has the same stability as the classical integral action, $\dot{\sigma} = -K_I \Delta q$, that is, they are all only stable. This means that the controller (11)-(14) should have faster convergence, better flexibility than the one (10), and then the controller (11)-(14) can yield higher performance of control, too. Moreover, integrator windup can be avoided by choosing suitable parameters K_{IP} and K_{ID} .

Discussion 3: Compared to the classical PID control and PD-NI control [5], the following observations can be made during the control process: when $K_{IP} f(\Delta q) + K_{ID} \Delta \dot{q} = 0$, the integral action remains constant; if the integral action is large, $\Delta \dot{q}$ increases, and then the integral action instantly decreases, vice versa. However, the integral action produced by the classical or nonlinear integrator [5] always increases as long as the error does not cross over zero, only when the error crosses over zero, the integral action will start to decrease. This shows that the control laws with the asymptotically stable integrator should have the faster convergence and better flexibility, and then can yield higher transient performance, once again.

4. Stability Analysis

For analyzing the stability of the closed-loop system, it is convenient to introduce the following notation.

$$\text{Defining } z(t) = \int_0^t f(\Delta q(\tau)) d\tau + K_{IP}^{-1} [g(q_d) - K_{ID} \Delta q(0)] ,$$

and then the control law (11) can be rewritten as,

$$\begin{aligned} u = & -(K_p + K_{ID})\Delta q - K_D\dot{q} \\ & - K_{pf}f(\Delta q) - K_{IP}z + g(q_d) \end{aligned} \quad (17)$$

The closed-loop system dynamics is obtained by substituting the control action u from (17) into the robot dynamic model (1),

$$\begin{aligned} M(q)\ddot{q} + C(q, \dot{q})\dot{q} + (K_D + D)\dot{q} + g(q) - g(q_d) \\ + (K_p + K_{ID})\Delta q + K_{IP}z + K_{pf}f(\Delta q) = 0 \end{aligned} \quad (18)$$

From the closed-loop system dynamics above, it is easy to see that the origin $(\Delta q^T, \dot{q}^T, z^T)^T = 0 \in R^{3n}$ is the unique equilibrium point.

Now, the objective is to provide conditions on the controller gains K_p , K_D , K_{pf} , K_{IP} and K_{ID} ensuring global asymptotic stability of the unique equilibrium point. This is established in the following.

Theorem: Consider the robot dynamics (1) together with control law (11). There exists positive constant a small enough, and choose the gain matrices K_p , K_D , K_{pf} , K_{IP} and K_{ID} such that

$$K_p + K_{ID} > K_{IP} + 4\lambda_M(M)I \quad (19)$$

$$\begin{aligned} U(q) - U(q_d) - \Delta q^T g(q_d) \\ + \frac{1}{4}\Delta q^T (K_p + K_{ID} - K_{IP})\Delta q \geq a \|\Delta q\|^2 \end{aligned} \quad (20)$$

$$\begin{aligned} f^T(\Delta q)[g(q) - g(q_d)] + f^T(\Delta q)K_{pf}f(\Delta q) \\ + f^T(\Delta q)(K_p + K_{ID} - K_{IP})\Delta q \\ \geq a \|f(\Delta q)\|^2 \end{aligned} \quad (21)$$

$$K_D + D > (\lambda_M(M) + C_M\sqrt{n}\beta)I \quad (22)$$

hold, and then the closed-loop system (18) is globally asymptotically stable, i.e. $\lim_{t \rightarrow \infty} \Delta q = 0$.

Proof: To carry out the stability analysis, we consider the following Lyapunov function candidate:

$$\begin{aligned} V = & \frac{1}{2}\dot{q}^T M(q)\dot{q} + \frac{1}{2}(z + \Delta q)^T K_{IP}(z + \Delta q) \\ & + U(q) - U(q_d) - \Delta q^T g(q_d) + f^T(\Delta q)M(q)\dot{q} \\ & + \frac{1}{2}\Delta q^T (K_p + K_{ID} - K_{IP})\Delta q \\ & + \sum_{i=1}^n \int_0^{\Delta q_i} f^T(x_i)(K_{pfi} + K_{Di} + D_i)dx_i \end{aligned} \quad (23)$$

where $x_i = \Delta q_i$; K_{pfi} , K_{Di} and D_i are the diagonal element of the matrices K_{pf} , K_D and D , respectively.

1) Positive definition of Lyapunov function candidate.

Now, considering the following inequality, and using (8), we have,

$$\begin{aligned} & \frac{1}{4}\dot{q}^T M(q)\dot{q} + \frac{1}{4}\Delta q^T (K_p + K_{ID} - K_{IP})\Delta q \\ & + f^T(\Delta q)M(q)\dot{q} \\ & = \frac{1}{4}[\dot{q} + 2f(\Delta q)]^T M(q)[\dot{q} + 2f(\Delta q)] \\ & - f^T(\Delta q)M(q)f(\Delta q) \\ & + \frac{1}{4}\Delta q^T (K_p + K_{ID} - K_{IP})\Delta q \\ & \geq \frac{1}{4}f^T(\Delta q)(K_p + K_{ID} - K_{IP} - 4\lambda_M(M)I)f(\Delta q) \end{aligned} \quad (24)$$

Substituting (20) and (24) into (23), and using (7) and (19), for any $(\Delta q^T, \dot{q}^T, z^T)^T \neq 0$, we obtain,

$$\begin{aligned} V = & \frac{1}{4}\dot{q}^T M(q)\dot{q} + a \|\Delta q\|^2 \\ & + \sum_{i=1}^n \int_0^{\Delta q_i} f^T(x_i)(K_{pfi} + K_{Di} + D_i)dx_i \\ & + \frac{1}{2}(z + \Delta q)^T K_{IP}(z + \Delta q) > 0 \end{aligned} \quad (25)$$

This shows that the Lyapunov function candidate (23) is positive definite.

2) Time derivative of Lyapunov function candidate.

The time derivative of Lyapunov function candidate (23) along the trajectories of the closed-loop system (18) is,

$$\begin{aligned} \dot{V} = & \dot{q}^T M(q)\ddot{q} + \frac{1}{2}\dot{q}^T \dot{M}(q)\dot{q} + (\dot{f}(\Delta q)\Delta \dot{q})^T M(q)\dot{q} \\ & + f^T(\Delta q)\dot{M}(q)\dot{q} + f^T(\Delta q)M(q)\ddot{q} \\ & + \dot{q}^T g(q) - \Delta \dot{q}^T g(q_d) + \Delta \dot{q}^T (K_p + K_{ID} - K_{IP})\Delta q \\ & + f^T(\Delta q)(K_{pf} + K_D + D)\Delta \dot{q} + (\dot{z} + \Delta \dot{q})^T K_{IP}(z + \Delta q) \end{aligned} \quad (26)$$

Substituting $\dot{z} = f(\Delta q)$, and $M(q)\ddot{q}$ from (18) into (26), and using (3), we have,

$$\begin{aligned} \dot{V} = & -\dot{q}^T (K_D + D)\dot{q} + (\dot{f}(\Delta q)\Delta \dot{q})^T M(q)\dot{q} \\ & + f^T(\Delta q)C(q, \dot{q})\dot{q} - f^T(\Delta q)[g(q) - g(q_d)] \\ & - f^T(\Delta q)(K_p + K_{ID} - K_{IP})\Delta q \\ & - f^T(\Delta q)K_{pf}f(\Delta q) \end{aligned} \quad (27)$$

Now, using (2) and (5), we get,

$$(\dot{f}(\Delta q)\Delta \dot{q})^T M(q)\dot{q} \leq \lambda_M(M) \|\dot{q}\|^2 \quad (28)$$

By using (4) and (9), we obtain,

$$f^T(\Delta q)C^T(q, \dot{q})\dot{q} \leq C_M\sqrt{n}\beta \|\dot{q}\|^2 \quad (29)$$

Incorporating (21), (28) and (29) into (27), we obtain,

$$\begin{aligned} \dot{V} \leq & -\dot{q}^T (K_D + D - \lambda_M(M)I - C_M\sqrt{n}\beta I)\dot{q} \\ & - a \|f(\Delta q)\|^2 \end{aligned} \quad (30)$$

From (22), (30) and $a > 0$, we can conclude $\dot{V} \leq 0$.

Using the fact that the Lyapunov function candidate (23) is a positive definite function and its time derivative is a negative semi-definite function, we conclude that the equilibrium point of the closed-loop system (18) is stable. In fact, $\dot{V} = 0$ means $\Delta q = 0$ and $\dot{q} = 0$. By invoking the LaSalle's invariance principle, it is easy to know that the equilibrium point $(\Delta q^T, \dot{q}^T)^T = 0$ is globally asymptotically stable, i.e., $\lim_{t \rightarrow \infty} \Delta q = 0$.

Remark 1: For the control laws (12)-(16), the globally asymptotically stable results can be derived under some similar sufficient conditions presented by (19)-(22). The proof can follow the similar argument and procedure. It is omitted because of the limited space.

Discussion 4: From the proof procedure above, it is easy to see that: 1) if we choose gain matrix, K_{ID} large enough, the linear term, $K_p \Delta q$, and the nonlinear term, $K_{pf} f(\Delta q)$, in the control law (11) is not necessary for guaranteeing global asymptotic stability of the closed-loop system and this means that the global asymptotic stability can still be ensured by the simplified form of the control law (11); 2) on the other hand, with the linear term, $K_p \Delta q$, and the nonlinear term, $K_{pf} f(\Delta q)$, it is obvious that the condition (19)-(21) is more easily satisfied and this results in that the control engineers have more freedom to choose the controller parameters, and then make them more easily tune a high performance controller.

5. Simulations

To illustrate the effect of the controller given in this paper, two-link manipulators shown in Figure 2 are considered. The dynamics (1) is of the following form [9]

$$\begin{cases} M_{11}\ddot{q}_1 + M_{12}\ddot{q}_2 + F_{11}\dot{q}_2^2 + 2F_{12}\dot{q}_1\dot{q}_2 + G_1 = u_1 \\ M_{12}\ddot{q}_1 + M_{22}\ddot{q}_2 + F_{11}\dot{q}_1^2 + 2F_{12}\dot{q}_1\dot{q}_2 + G_2 = u_2 \end{cases}$$

where: $M_{11} = (m_1 + m_2)l_1^2 + m_2l_2^2 + 2m_2l_1l_2 \cos(q_2)$,
 $M_{22} = m_2l_2^2$, $M_{12} = m_2l_2^2 + m_2l_1l_2 \cos(q_2)$,
 $F_{11} = F_{12} = -m_2l_1l_2 \sin(q_2)$,
 $G_1 = (m_1 + m_2)gl_1 \sin(q_1) + m_2gl_2 \sin(q_1 + q_2)$
 $G_2 = m_2gl_2 \sin(q_1 + q_2)$.

The normal parameter values of the system are selected as: $m_1 = m_2 = 1kg$, $l_1 = l_2 = 1m$, $g = 10m/s^2$.

The desired (set point) positions are chosen as:
 when $t < 10s$, $q_{d1} = 1, q_{d2} = -1$;
 when $10s \leq t < 20s$, $q_{d1} = 3, q_{d2} = 2$;
 when $t \geq 20s$, $q_{d1} = q_{d2} = 0$.

The simulation is implemented by using the control laws (11) and (14), respectively. In simulation, Arimoto

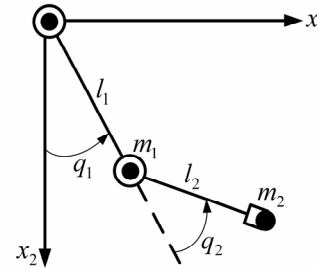


Figure 2. The two-link robot manipulators.

sine function (6) is used as the nonlinear function of the control laws.

The gain matrices of the control law (11) are selected as:
 $K_p = \text{diag}(310,310)$, $K_D = \text{diag}(150,150)$,
 $K_{IP} = \text{diag}(500,500)$, $K_{ID} = \text{diag}(200,200)$,
 and $K_{pf} = \text{diag}(100,100)$.

The gain matrices of the control law (14) are given as:
 $K_D = \text{diag}(60,30)$, $K_{IP} = \text{diag}(1000,500)$,
 and $K_{ID} = \text{diag}(1250,600)$.

The simulations with sampling period of 2ms are implemented. Figures 3 and 5 present the response of the robot manipulators under the normal parameters. Figures 4 and 6 are the simulation results under the case that the mass $m_2 = 1kg$ is substituted for $m_2 = 3kg$ when $10s \leq t < 20s$, corresponding to moving payload of 2kg.

From the simulation results, it is easy to see that:

- 1) The optimum response can all be achieved, respectively, by the control laws (11) and (14) with a set of control parameters in the whole domain of interest, even under the case that the payload is changed abruptly;
- 2) These two controllers used in simulation all have the faster convergence, better flexibility and stronger robustness with respect to uncertain payload, which means that the controllers (12) and (13) should have the same high performance of control as the controllers (11) and (14) because they all employ the same integrators;
- 3) Comparing the Figures 3 and 5, the controller (11) is easier to achieve the control of high speed and high performance than the controller (14) because the former has two freedom parameters.

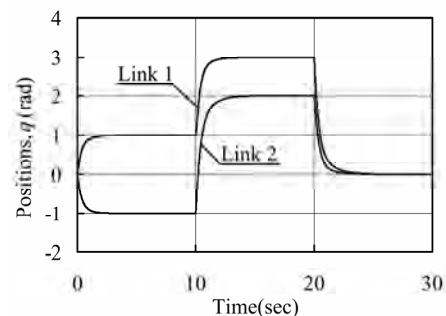


Figure 3. Under normal parameters, the simulation results with controller (11).

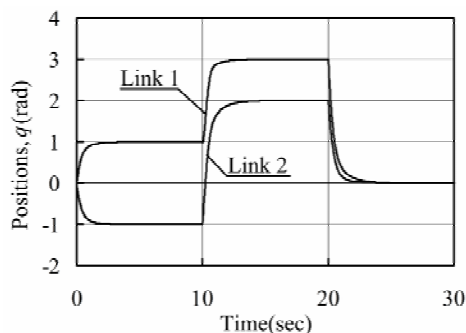


Figure 4. Under perturbed parameters, corresponding to moving payload, the simulation results with controller (11).

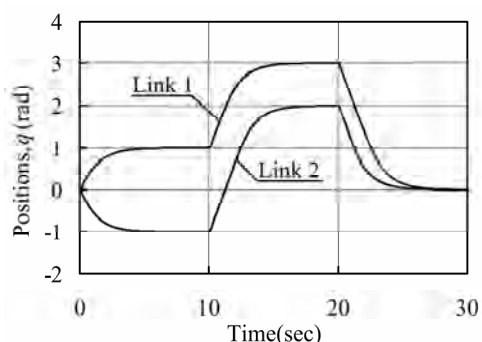


Figure 5. Under normal parameters, the simulation results with controller (14).

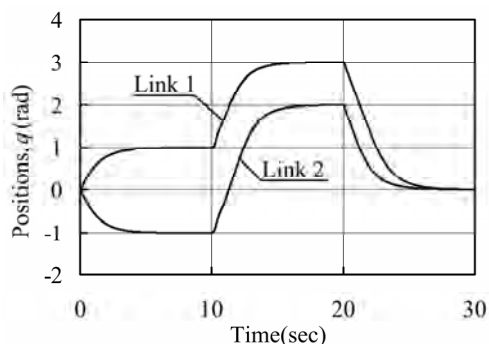


Figure 6. Under perturbed parameters, corresponding to moving payload, the simulation results with controller (14).

6. Conclusions

In this paper, we have presented a set of solution to the problem of set point regulation for rigid robots without

exact knowledge of the payload. An attractive feature of our scheme is that the control laws with the asymptotically stable integrators have the faster convergence, better flexibility and stronger robustness with respect to uncertain and varying-time payload, and then the optimum response can be achieved. The explicit conditions on the regulator gains to ensure global asymptotic stability of the overall closed-loop system are given in terms of some information exacted from the robot dynamics. Our findings have been corroborated numerically on a two DOF vertical robot manipulators.

7. References

- [1] Y. X. Su, *Nonlinear Control Theory for Robot Manipulators*, Science Publishing, Beijing, 2008.
- [2] J. Alvarez-Ramirez, I. Gervantes, and R. Kelly, "PID regulation of robot manipulators: Stability and performance," *System & Control Letters*, Vol. 41, No. 2, pp. 73–83, April 2000.
- [3] A. A. Pervozvanski and L. B. Freidovich, "Robust stability of robotic Manipulators by PID controllers," *Dynamics and Control*, Vol. 9, No. 3, pp. 203–222, September 1999.
- [4] S. Arimoto, "A class of quasi-natural potentials and Hyper-stable PID servo-loops for nonlinear robotic system," *Transactions of the Society of Instrument and Control Engineers*, Vol. 30, No. 9, pp. 1005–1012, September 1994.
- [5] R. Kelly, "Global positioning of robotic manipulators via PD control plus a class of nonlinear integral actions," *IEEE Transactions on Automatic Control*, Vol. 43, No. 7, pp. 934–938, July 1998.
- [6] R. Ortega, A. Loria, and R. Kelly, "A semiglobally stable output feedback PI^2D regulator for robot manipulators," *IEEE Transactions on Automatic Control*, Vol. 40, No. 8, pp. 1432–1436, August 1995.
- [7] B. S. Liu and F. C. Lin, "A semiglobally stable $PD-I^{PD}$ regulator for robot manipulators," to be published in 2009 International Conference on Measuring Technology and Mechatronics Automation proceeding.
- [8] B. S. Liu and B. L. Tian, "A globally stable $PD-I^{NP-D}$ regulator for robot manipulators," to be published in 2009 International Conference on Information Technology and Computer Science proceedings.
- [9] S. J. Yu, X. D. Qi, and J. H. Wu, *Iterative Learning Control Theory & Application*, Machine Publishing, Beijing, 2005.

Focusing of Azimuthally Polarized Hyperbolic-Cosine-Gaussian Beam

Xiumin Gao^{1,2}, Mingyu Gao¹, Song Hu¹, Hanming Guo², Jian Wang¹, Songlin Zhuang²

¹Electronics & Information College, Hangzhou Dianzi University, Hangzhou, China

²University of Shanghai for Science and Technology, Shanghai, China

E-mail: xiumin_gao@yahoo.com.cn, optics.hangzhou@gmail.com, husong1971@hotmail.com

Received October 3, 2009; revised November 2, 2009; accepted November 8, 2009

Abstract

The focusing properties of azimuthally polarized hyperbolic-cosine-Gaussian (ChG) beam are investigated theoretically by vector diffraction theory. Results show that the intensity distribution in focal region of azimuthally polarized ChG beam can be altered considerably by decentered parameters, and some novel focal patterns may occur for certain case. On increasing decentered parameters, ring shape of focal pattern can evolve into four-peak focal pattern, and azimuthal field component affects focal pattern more significantly than radial field component. Optical gradient force is also calculated to show that the focusing properties may be used in optical tweezers technique.

Keywords: Focusing Properties, Hyperbolic-Cosine-Gaussian Beam, Vector Diffraction Theory

1. Introduction

Laser beams with cylindrical symmetry in polarization have attracted many researchers recently for their interesting properties and applications. And these beams are called cylindrical vector beams and can be generated by active or passive methods [1–4]. Due to the polarization symmetry, the electric field at the focus has unique polarization properties. K. S. Youngworth and T. G. Brown calculated cylindrical-vector fields [2], which shows that, in the particular case of a tightly focused radially polarized beam, the polarization shows large inhomogeneities in the focal region, while the azimuthally polarized beam has purely transverse field in focal region. Focus shaping technique is also reported by using generalized cylindrical vector beams [3], in which a generalized cylindrical vector beam can be decomposed into radially polarized and azimuthally polarized components. And a generalized cylindrical beam can be generated from a radially polarized or an azimuthally polarized light using a two-half-wave-plate polarization rotator.

On the other hand, although Gaussian beam is familiar to researchers, it is only one kind of solution of the Helmholtz equation. The more general solution is Hermite-Sinusoidal-Gaussian beams, which was introduced by Casperson and coworkers [5,6]. Hyperbolic-cosine-Gaussian beams are regarded as the special case of Hermite-sinusoidal-Gaussian beams, and are of practical interest because their profiles can be altered by

choosing suitable beam parameters in cosh parts [7]. Propagation and focusing properties of hyperbolic-cosine-Gaussian beams have become the object of some works [8–12]. To investigate focusing properties of this kind of light beam with azimuthally polarized distribution is very interesting, which may deepen understanding of its properties and expand application. In this paper, the focusing properties of the azimuthally polarized hyperbolic-cosine-Gaussian (ChG) beam are investigated theoretically by vector diffraction theory. In Section 2, the principle of the focusing system is given. And results and discussions are shown in Section 3. Conclusions are summarized in Section 4.

2. Principle of the Focusing Azimuthally Polarized ChG Beam

In the focusing system we investigated, focusing beam is azimuthally polarized ChG beam whose value of transverse optical field is same as that of the scalar ChG beam, and its polarization distribution turns on azimuthally symmetric. Therefore, in the cylindrical coordinate system $(r, \phi, 0)$ the field distribution $\vec{E}(r, \phi, 0)$ of the azimuthally polarized ChG beam is written as [1–3],

$$\vec{E}_0(r, \phi, 0) = E_0(r, \phi, 0) \cdot \vec{n} \quad (1)$$

where \vec{n} is the azimuthal unit vector of polarized direction. Term $E_0(r, \phi, 0)$ is optical field value distribu-

tion and can be written in the form [7–9],

$$E(x, y, 0) = B \cosh(\Omega_x x) \cosh(\Omega_y y) \exp\left(-\frac{x^2 + y^2}{\omega_0^2}\right) \quad (2)$$

where \cosh is hyperbolic-cosine function, ω_0 is the waist width of the beam. And B is a constant. Ω_x and Ω_y indicate decentered parameters of ChG beam. According to vector diffraction theory, the electric field in focal region of azimuthally polarized ChG beam is [13],

$$\vec{E}(\rho, \phi, z) = E_\rho \vec{e}_\rho + E_\phi \vec{e}_\phi \quad (3)$$

where \vec{e}_ρ and \vec{e}_ϕ are the unit vectors in the radial and azimuthal directions, respectively. To indicate the position in image space, cylindrical coordinates (ρ, ϕ, z) with origin $\rho = z = 0$ located at the paraxial focus are employed. E_ρ and E_ϕ are the amplitudes of two orthogonal components and can be expressed as:

$$E_\rho(\rho, \phi, z) = \frac{iA}{\pi} \int_0^\alpha \int_0^{2\pi} \sqrt{\cos\theta} \cdot E_0 \cdot \sin\theta \sin(\varphi - \phi) \cdot \exp\{ik[z \cos\theta + \rho \sin\theta \cos(\varphi - \phi)]\} d\varphi d\theta \quad (4)$$

$$E_\phi(\rho, \phi, z) = \frac{-iA}{\pi} \int_0^\alpha \int_0^{2\pi} \sqrt{\cos\theta} \cdot E_0 \cdot \sin\theta \cos(\varphi - \phi) \cdot \exp\{ik[z \cos\theta + \rho \sin\theta \cos(\varphi - \phi)]\} d\varphi d\theta \quad (5)$$

where θ and φ denote the tangential angle with respect to the z axis and the azimuthal angle with respect to the x axis, respectively. k is wave number. $\alpha = \arcsin(NA)$ is convergence angle corresponding to the radius of incident optical aperture. In order to make focusing properties clear and simplify calculation process, after simple derivation, Equation 2 can be rewritten as [11]:

$$E(\theta, \varphi) = B \cdot \cosh[NA^{-1} \cdot \beta_x \cdot \sin(\theta) \cdot \cos(\varphi)] \cdot \cosh[NA^{-1} \cdot \beta_y \cdot \sin(\theta) \cdot \sin(\varphi)] \cdot \exp\left[-\frac{\sin^2(\theta)}{NA^2 \cdot w^2}\right] \quad (6)$$

where $w = \omega_0/r_0$ is called relative waist width. Parameters $\beta_x = r_p \Omega_x$ and $\beta_y = r_p \Omega_y$ in this paper are called decentered parameters of azimuthally polarized ChG beam. Substitute the Equation 6 into Equations 4 and 5, we can obtain:

$$E_\rho(\rho, \phi, z) = \frac{iAB}{\pi} \int_0^\alpha \int_0^{2\pi} \sqrt{\cos\theta} \sin\theta \sin(\varphi - \phi) \cdot \cosh[NA^{-1} \cdot \beta_x \cdot \sin(\theta) \cdot \cos(\varphi)] \cdot \exp(i\psi) \cdot \cosh[NA^{-1} \beta_y \sin(\theta) \sin(\varphi)] \cdot \exp\left[-\frac{\sin^2(\theta)}{NA^2 \cdot w^2}\right]$$

$$\cdot \exp\{ik[z \cos\theta + \rho \sin\theta \cos(\varphi - \phi)]\} d\varphi d\theta \quad (7)$$

$$E_\phi(\rho, \phi, z) = \frac{-iAB}{\pi} \int_0^\alpha \int_0^{2\pi} \sqrt{\cos\theta} \sin\theta \cos(\varphi - \phi) \cdot \cosh[NA^{-1} \cdot \beta_x \cdot \sin(\theta) \cdot \cos(\varphi)] \cdot \exp(i\psi) \cdot \cosh[NA^{-1} \beta_y \sin(\theta) \sin(\varphi)] \cdot \exp\left[-\frac{\sin^2(\theta)}{NA^2 \cdot w^2}\right] \cdot \exp\{ik[z \cos\theta + \rho \sin\theta \cos(\varphi - \phi)]\} d\varphi d\theta \quad (8)$$

The optical intensity in focal region is proportional to the modulus square of Equation 3. Based on the above equations, focusing properties of azimuthally polarized ChG beam can be investigated in detail.

3. Results and Discussions

Without loss of validity and generality, it was supposed that $NA=0.95$ and $w=1$. Firstly, the intensity distributions in focal region of azimuthally polarized ChG beam under condition of different decentered parameters are calculated and illustrated in Figure 1. It should be noted that $\beta = \beta_x = \beta_y$, and the distance unit in all figures in this paper is k^{-1} , where k is the wave number of incident beam. The azimuthal angle ranges from $-\pi$ to π in azimuthal coordinate. It can be seen from Figure 1 that the intensity distribution turns on one ring shape in focal plane for small decentered parameter β , which is similar to that for Gaussian beam. On increasing β , the focal pattern changes very remarkably, from one ring focal pattern to four-peak focal pattern, and these four intensity peaks overlap very considerably, as shown in Figure 1(b). Increase decentered parameter β continuously, there appear several weak overlapping intensity peaks outside of the center four-peak overlapping focal pattern, in addition, multiple dark focal spots occur between inner four-peak focal pattern and outer multiple overlapping intensity pattern. And dark focal spots get more obvious on increasing β , such as in Figure 1(f). From above focal pattern evolution, we can see that intensity distribution in focal region of azimuthally polarized ChG beam can be altered considerably by decentered parameters, and some novel focal patterns may occur.

In order to understand the focusing properties deeply, the different optical field components in focal region are also investigated. And one calculation example is given here. Figure 2 illustrates the radial field component for $\beta=2$ and $\beta=17$, and the corresponding azimuthal field component is given in Figure 3.

The radial field component distribution turns multiple optical intensity peaks outside of optical axis, and changes slightly under condition of different β . While, azimuthal field component distribution changes very considerably on increasing β , evolving from one focal ring pattern to multiple overlapping optical intensity peaks in focal plane.

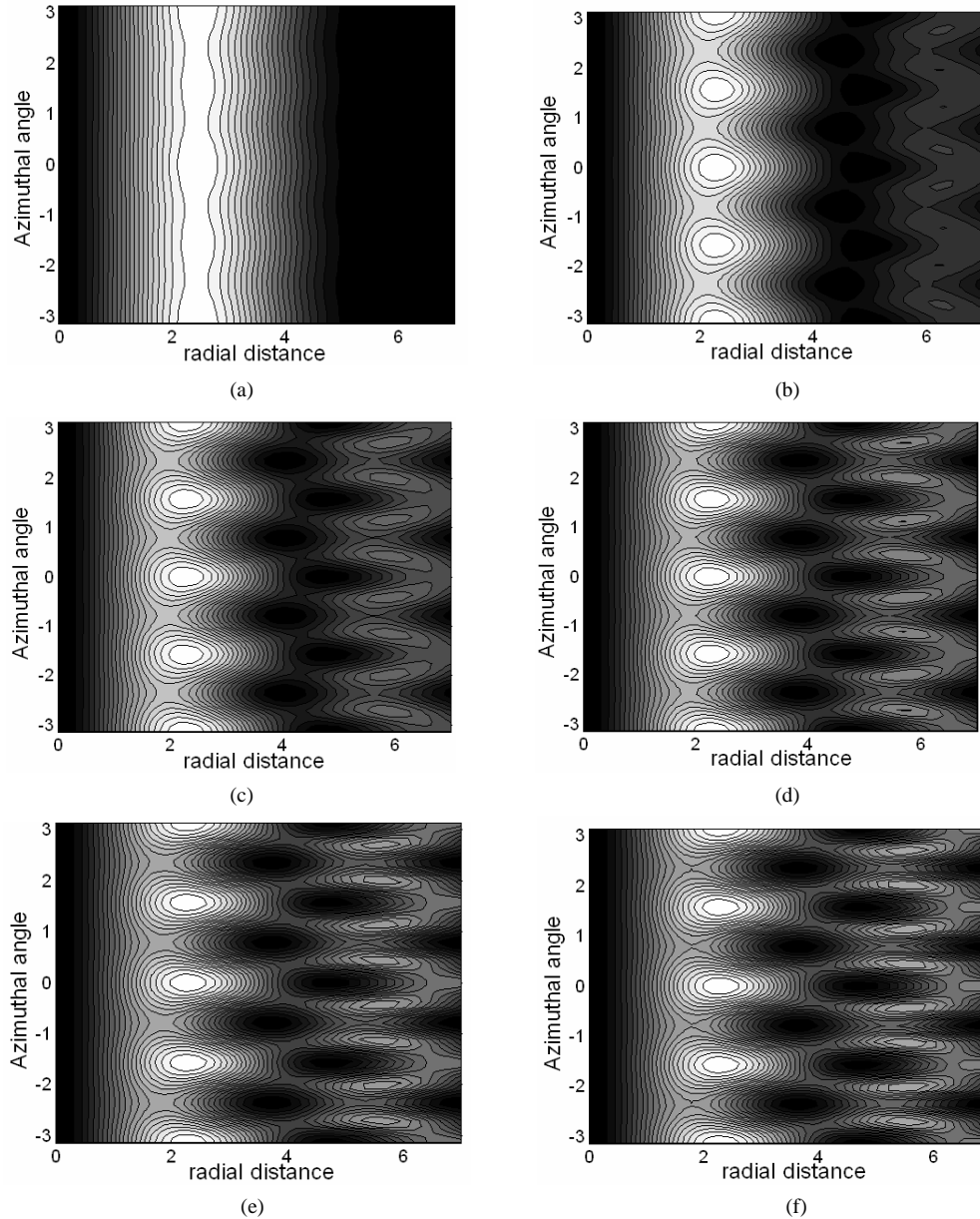


Figure 1. Intensity distributions in focal region for (a) $\beta=2$, (b) $\beta=5$, (c) $\beta=8$, (d) $\beta=11$, (e) $\beta=14$, and (f) $\beta=17$, respectively.

By comparing Figures 2 and 3 with Figure 1, it can be seen that azimuthal field component distribution is very similar to total focal pattern. Therefore, azimuthal field component affects focal pattern more significantly than radial field component, namely, azimuthal field component decides optical intensity distribution in focal region of the azimuthally polarized ChG beam.

Now, the possible application of focusing of azimuthally polarized ChG beam is discussed. Optical tweezers have been increasingly valuable tool for research and accelerated many major advances in numerous areas of science [14–17]. In optical tweezers system, it is usually deemed that the forces exerted on the particles in light field include two kinds of forces, one is the gradient

force, which is proportional to the intensity gradient; the other is the scattering force, which is proportional to the optical intensity [16]. So, the tunable focal pattern predicts that the optical trap may be controllable. The gradient force trap is necessary condition for constructing the optical trap and can be expressed as [16]

$$F_{grad} = \frac{n_b^2 r^3}{2} \cdot \left(\frac{m^2 - 1}{m^2 + 2} \right) \nabla |\vec{E}(\rho, \phi, z)|^2 \quad (9)$$

where r is the radius of trapped particles, n_b is the refraction index of the surrounding medium, and m , the relative index of refraction, equals to the ratio of the refraction index of the particle n_p to the refraction index of the

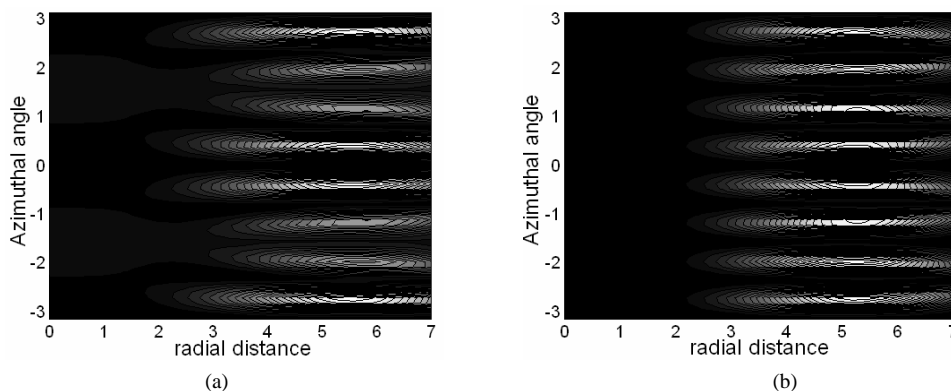


Figure 2. Radial field component for (a) $\beta=2$ and (b) $\beta=17$, respectively.

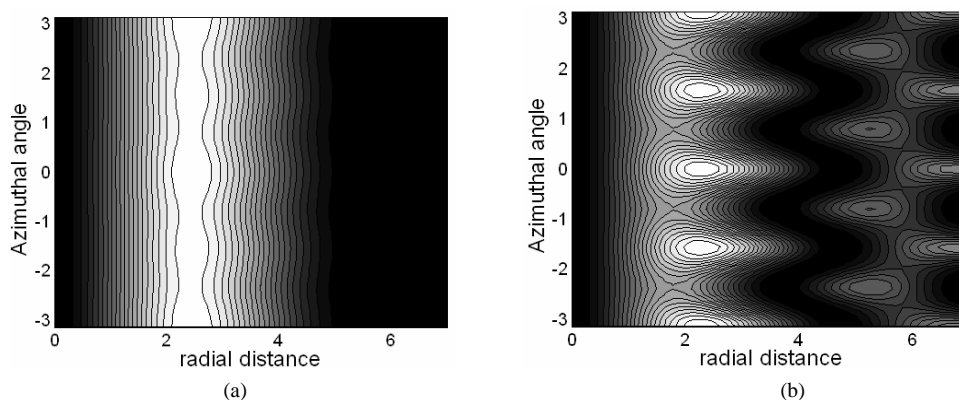


Figure 3. Azimuthal field component for (a) $\beta=2$ and (b) $\beta=17$, respectively.

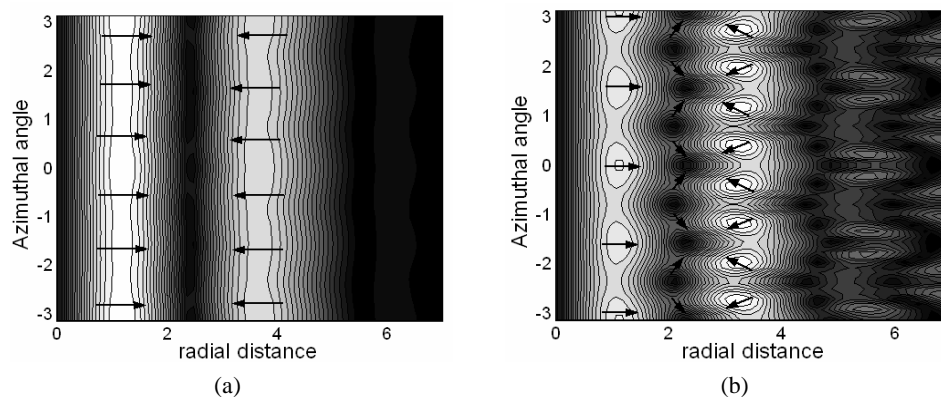


Figure 4. Optical gradient force for (a) $\beta=2$ and (b) $\beta=5$, respectively. The arrows indicate the direction of optical gradient force in focal region.

surrounding medium n_b . Gradient force F_{grad} points in the direction of the gradient of the light intensity for $n_p > n_b$. The optical gradient force can be computed numerically by substituting Equation 3 into Equation 9. Figure 4 illustrates the optical gradient force for $\beta=2$ and $\beta=5$. The arrows indicate the direction of optical gradient force in focal region. There is one ring optical trap for $\beta=2$, and multiple optical traps under condition of $\beta=5$. Decentered parameters can change focal pattern very remarkable. Therefore, the focusing properties of azimuthally polarized ChG beam can be constructed to tunable optical traps.

4. Conclusions

The focusing properties of azimuthally polarized ChG beam are investigated theoretically by vector diffraction theory. Simulations results show that the intensity distribution in focal region of azimuthally polarized ChG beam can be altered considerably by decentered parameters and some novel focal patterns may occur. For instance, ring focal pattern, four-peak focal pattern, and dark focal spot. On increasing decentered parameters, ring shape of focal pattern can evolve into four-peak fo-

cal pattern, which may be used to construct tunable optical tweezers. In addition, azimuthal field component affects focal pattern more significantly than radial field component.

5. Acknowledgments

This work was supported by National Basic Research Program of China (2005CB724304), National Natural Science Foundation of China (60708002, 60807007, 60871088, 60778022), China Postdoctoral Science Foundation (20080430086), Shanghai Postdoctoral Science Foundation of China (08R214141), and Shanghai Leading Academic Discipline Project (S30502).

6. References

- [1] Q. Zhan, "Cylindrical vector beams: From mathematical concepts to applications," *Advances in Optics and Photonics*, Vol. 1, pp. 1–57, 2009.
- [2] K. S. Youngworth and T. G. Brown, "Focusing of high numerical aperture cylindrical-vector beams," *Optics Express*, Vol. 7, pp. 77–87, 2000.
- [3] X. Gao, J. Wang, H. Gu, and W. Xu, "Focusing properties of concentric piecewise cylindrical vector beam," *Optik*, Vol. 118, pp. 257–265, 2007.
- [4] G. Zhou, Y. Ni, and Z. Zhang, "Analytical vectorial structure of non-paraxial nonsymmetrical vector Gaussian beam in the far field," *Optics Communications*, Vol. 272, pp. 32–39, 2007.
- [5] L. W. Casperson, D. G. Hall, and A. A. Tovar, "Sinusoidal-Gaussian beams in complex optical systems," *Journal of Optical Society of America A*, Vol. 14, pp. 3341–3348, 1997.
- [6] L. W. Casperson and A. A. Tovar, "Hermite-sinusoidal-Gaussian beams in complex optical systems," *Journal of Optical Society of America A*, Vol. 15, pp. 954–961, 1998.
- [7] X. Du and D. Zhao, "Elliptical cosh-Gaussian beams," *Optics Communications*, Vol. 265, pp. 418–424, 2006.
- [8] Z. Hricha and A. Belafhal, "Focusing properties and focal shift in hyperbolic-cosine-Gaussian beams," *Optics Communications*, Vol. 253, pp. 242–249, 2005.
- [9] B. Lu and S. Luo, "Beam propagation factor of hard-edge diffracted cosh-Gaussian beams," *Optics Communications*, Vol. 178, pp. 275–281, 2000.
- [10] B. Lu, H. Ma, and B. Zhang, "Propagation properties of cosh-Gaussian beams," *Optics Communications*, Vol. 164, pp. 165–170, 1999.
- [11] X. Gao, "Focusing properties of the hyperbolic-cosine-Gaussian beam induced by phase plate," *Physics Letters A*, Vol. 360, pp. 330–335, 2006.
- [12] X. Gao and J. Li, "Focal shift of apodized truncated hyperbolic-cosine-Gaussian beam," *Optics Communications*, Vol. 273, pp. 21–27, 2007.
- [13] S. Sato and Y. Kozawa, "Hollow vortex beams," *Journal of Optical Society of America A*, Vol. 26, pp. 142–146, 2009.
- [14] M. P. MacDonald, L. Paterson, K. V. Sepulveda, J. Arlt, W. Sibbett, and K. Dholakia, "Creation and manipulation of three-dimensional optically trapped structures," *Science*, Vol. 296, pp. 1101–1103, 2002.
- [15] D. G. Grier, "A revolution in optical manipulation," *Nature*, Vol. 424, pp. 810–816, 2003.
- [16] V. Garcés-Chaves, D. McGloin, H. Melville, W. Sibbett, and K. Dholakia, "Simultaneous micromanipulation in multiple planes using a self reconstructing light beam," *Nature*, Vol. 419, pp. 145–147, 2002.
- [17] K. Visscher and G. J. Brakenhoff, "Theoretical study of optically induced forces on spherical particles in a single beam trap I: Rayleigh scatterers," *Optik*, Vol. 89, pp. 174–180, 1992.

Call for Papers

ENGINEERING

A Journal Published by Scientific Research Publishing, USA

www.scirp.org/journal/eng

Editor-in-Chief

Prof. David L. Carroll Wake Forest University, USA

Editorial Board

Prof. Alain Bernard
Prof. Hongbin Sun
Prof. Chengshan Wang
Prof. Xiangjun Zeng
Prof. Luowei Zhou
Dr. Hongyu Zhang
Dr. Wei Yan
Dr. Hongyang Chen
Prof. Ming Chen
Prof. Chui-Chi Lee
Prof. Zhao Xu
Prof. Jae Mung Kim
Prof. Baolin Wang
Prof. Shahnor Basri
Prof. Tsutomu Yoshihara
Prof. John Marsh
Prof. Gaofeng Wang
Dr. Koduri Venkata Surya Ramam
Dr. Rahat Iqbal
Dr. Rehan Ahmed
Dr. P. Chandramohan
Dr. Mehرداد Massoudi
Prof. MOH'D A. M. AL-NIMR
Dr. V. P. Yashnikov
Prof. Yong-Gang Lv
Prof. Jan Awrejcewicz
Prof. Shouetsu Itou
Prof. Sergey M. Smolskiy

Ecole Centrale de Nantes, France
Tsinghua University, China
Tianjin University, China
Changsha University of Science and Technology, China
Chongqing University, China
Ceres Inc., Thousand Oaks, CA, USA
Trend Micro, USA
The University of Tokyo, Japan
Southeast University, China
SHU-TE University, Taiwan (China)
Technical University of Denmark, Denmark
INHA University Incheon, Korea (South)
Harbin Institute of Technology, China
Universiti Putra Malaysia Selangor, Malaysia
Waseda University, Japan
IEEE Photonics Society, UK
Wuhan University, China
Universidad of Concepcion, Chile
Coventry University, UK
Heriot-Watt University, UK
Anna University, India
U. S. Department of Energy/NETL-Pittsburgh, USA
Jordan University of Science and Technology, Jordan
Russian Academy of Sciences, Russia
Chongqing University, China
Department of Automatics and Biomechanics (DAB), TUL, Poland
Kanagawa University, Japan
Moscow Power Engineering University, Russia



ENGINEERING is an international journal dedicated to the latest advancement of engineering. The goal of this journal is to provide a platform for engineers and academicians all over the world to promote, share, and discuss various new issues and developments in different areas of engineering. All manuscripts must be prepared in English, and are subject to a rigorous and fair peer-review process. Accepted papers will immediately appear online followed by printed hard copy. The journal publishes original papers including but not limited to the following fields:

- Aerospace Engineering
- Agricultural Engineering
- Chemical Engineering
- Civil Engineering
- Electrical Engineering
- Environmental Engineering
- Industrial Engineering
- Materials Engineering
- Mechanical Engineering
- Mining Engineering
- Nanotechnology
- Nuclear Engineering
- Power Engineering
- Test Engineering
- Transportation Engineering

We are also interested in: 1) Short Reports—2-5 page papers where an author can either present an idea with theoretical background but has not yet completed the research needed for a complete paper or preliminary data; 2) Book Reviews—Comments and critiques.

★ Notes for Intending Authors

Submitted papers should not be previously published nor be currently under consideration for publication elsewhere. Paper submission will be handled electronically through the website. For more details, please access the website.

★ Website and E-Mail

<http://www.scirp.org/journal/eng>

eng@scirp.org

TABLE OF CONTENTS

Volume 2 Number 2

February 2010

Experimental Study of Stacked Rectangular Microstrip Antenna for Dual-Band R. K. Vishwakarma, S. Tiwari.....	85
Analysis of Rectangular Notch Antenna for Dual-Band Operation R. K. Vishwakarma, S. Tiwari.....	91
The Quantized Characterization of Cooked Rice Hardness and Research on the Automatic Measurement Technology N. Jiang, Y. Gao, J. P. Zhou, L. Q. Gao, J. H. Zhou, Q. G. Dai.....	97
Analytic Computation Method of the Equivalent Thickness of Superposition Multi-Throttle-Slices of Twin-Tubes Shock Absorber C. C. Zhou, Y. Z. Xu.....	103
Sliding Mode Control with Auto-Tuning Law for Maglev System L. L. Zhang, Z. Z. Zhang, Z. Q. Long, A. Hao.....	107
The Research on Adaptive Control Modeling of a Liquid Fertilizer Spreader Z. D. Yang.....	113
A Set of Globally Stable N-PID Regulators for Robotic Manipulators B. S. Liu, F. C. Lin, B. L. Tian.....	118
Focusing of Azimuthally Polarized Hyperbolic-Cosine-Gaussian Beam X. M. Gao, M. Y. Gao, S. Hu, H. M. Guo, J. Wang, S. L. Zhuang.....	124

